2007-09-06

Development of a Method for Calculating Delta Scuti Rotational Velocities and Hydrogen Beta Color Indices

Tabitha Christi Buehler

Brigham Young University - Provo

DEVELOPMENT OF A METHOD FOR CALCULATING DELTA

SCUTI ROTATIONAL VELOCITIES AND HYDROGEN-BETA

COLOR INDICES

by

Tabitha Christi Bush

A thesis submitted to the faculty of

Brigham Young University

in partial fulfillment of the requirements for the degree of

Master of Science

Department of Physics and Astronomy

Brigham Young University

December 2007

BRIGHAM YOUNG UNIVERSITY

GRADUATE COMMITTEE APPROVAL

of a thesis submitted by

Tabitha Christi Bush

This thesis has been read by each member of the following graduate committee and by majority vote has been found to be satisfactory.

_____	_____
Date	Eric G. Hintz, Chair
_____	_____
Date	Michael D. Joner
_____	_____
Date	Benjamin J. Taylor
_____	_____
Date	J. Ward Moody

BRIGHAM YOUNG UNIVERSITY

As chair of the candidate's graduate committee, I have read the thesis of Tabitha Christi Bush in its final form and have found that (1) its format, citations, and bibliographical style are consistent and acceptable and fulfill university and department style requirements; (2) its illustrative materials including figures, tables, and charts are in place; and (3) the final manuscript is satisfactory to the graduate committee and is ready for submission to the university library.

_____
Date

_____
Eric G. Hintz
Chair, Graduate Committee

Accepted for the Department

_____
J. Ward Moody, Graduate Coordinator
Department of Physics and Astronomy

Accepted for the College

_____
Thomas W. Sederberg, Associate Dean
College of Physical and Mathematical Sciences

ABSTRACT

DEVELOPMENT OF A METHOD FOR CALCULATING DELTA

SCUTI ROTATIONAL VELOCITIES AND HYDROGEN-BETA

COLOR INDICES

Tabitha Christi Bush

Department of Physics and Astronomy

Master of Science

To add to the understanding of the structure and evolution of δ Scuti stars, 167 δ Scutis north of -01° declination and brighter than 13th magnitude have been observed spectroscopically. A method for calculating rotational velocity values and Hβ color indices for the stars in the data set with no previously published values is developed, using the stars in the data set brighter than 7th magnitude. Rotational velocity values for four stars with previously unknown values and Hβ index values for five stars with previously unknown values are calculated.

ACKNOWLEDGMENTS

Contents

List of Tables

List of Figures

Chapter 1

Introduction and Background

1.1 Project Motivation

Many aspects of stellar evolution remain a puzzle. In order to more completely understand stellar evolution, several pieces must be put together. It is not possible to observe one star go through its whole life process, so stars at different stages of evolution must be studied. Also, different characteristics about stars such as temperature, composition, motion, distance, rotation, and radius are studied and related to each other in order to gain an understanding of the structure and evolution of these stars.

Delta Scuti stars have been studied by the Brigham Young University Astronomy Research Group for many years. This subclass of variable stars represents a particular stage of stellar evolution. Rodriguez et al. (2000) compiled a list of the δ Scuti stars known at the time along with each star's pulsation period, pulsation amplitude, visual magnitude, projected rotational velocity, radial velocity, spectral type, and different color index values. This catalog contains 636 δ Scuti stars, 417 of which are brighter than 13th magnitude. Only 191 stars out of 636, or about 30%, have projected rotational velocity values listed. For the stars brighter than 13th magnitude, 188 stars, or about 45%, have no projected rotational velocity values listed. In addition, about 20% of the δ Scuti stars brighter than 13th magnitude do not list an Hβ color index.

Strong relations between rotational velocity and pulsation properties of δ Scutis, such as amplitude and mode, have been found, as discussed by Breger et al. (2007). Figure 1.1 shows the relation in δ Scutis between rotational velocity and pulsation amplitude. The stars along the vertical line on the left-hand side of the plot are known as High-Amplitude Delta Scutis (HADS). Along the bottom of the plot
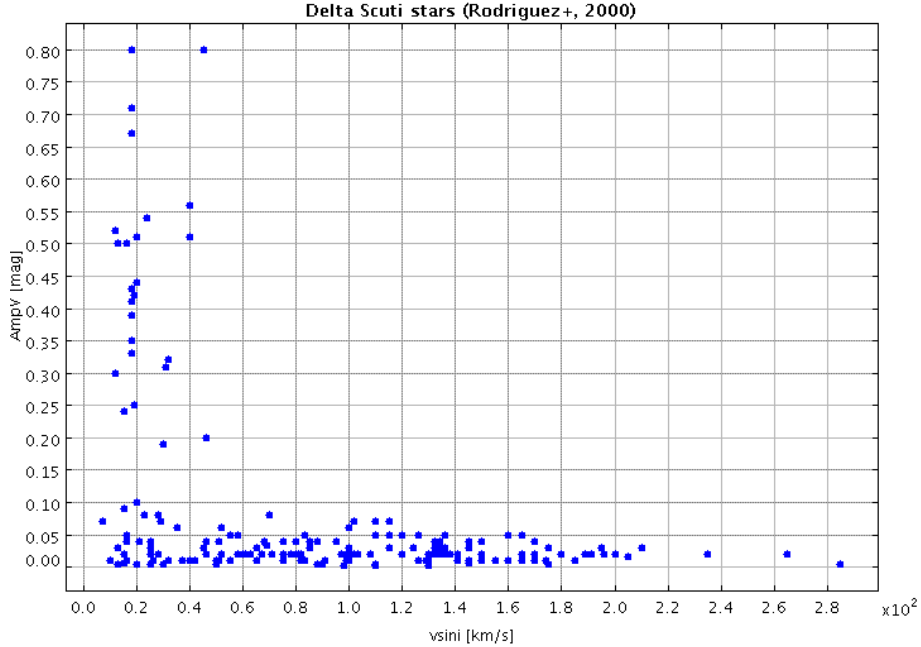
Figure 1.1: $v \sin i$ vs. pulsation amplitude for δ Scutis in Rodriguez (2000) catalog

are the Low-Amplitude Delta Scutis (LADS). The seven stars in Figure 1.1 near the left-hand trend that don't seem fit either of these trends are in some kind of medium-amplitude range with slow rotational velocities. Studying δ Scutis in this region may significantly add to the understanding of the structure and evolution of this group of variable stars. Also, the relation between rotational velocity and pulsation mode can aid in the study of asteroseismology. This study of global oscillations inside stars is being pursued by current projects such as the Canadian MOST telescope and the Stellar Oscillations Network Group (SONG).

Another interesting relation has been revealed by McNamara (2007), between projected rotational velocity and (B-V) color index. Figure 1.2 is a representation of (B-V) index values for δ Scutis across the Instability Strip. As shown in Figure 1.2, slow rotating δ Scuti stars seem to be missing from the blue edge of the distribution– there is a gap in the plot between (B-V) values of about 0.14 to 0.20 and for $v \sin i$ values up to about 120 km/s. This gap could be due to selection, or there could be

2
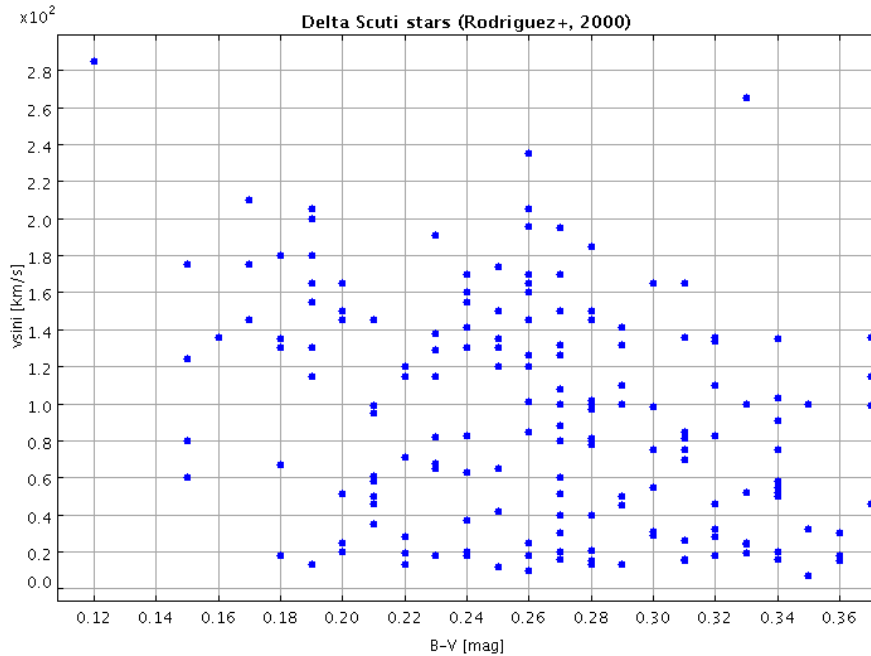
Figure 1.2: (B-V) color index vs. $v \sin i$ for δ Scutis in Rodriguez (2000) catalog

a physical mechanism that explains it. Perhaps the temperatures in the gap are too high to characterize δ Scutis.

1.2 Delta Scuti Stars

Variable stars are stars that change periodically in their light output over time. There are two main classifications of variable stars: line-of-sight variables and intrinsic variables. Line-of-sight variable stars are stars that appear to be varying in their light output because of their position relative to observation from Earth. For example, an eclipsing binary star system is one that would appear from Earth to be periodically changing in its light output as one star eclipses the other. Intrinsic variables, such as δ Scutis, are stars that are varying due to some physical mechanism inside the star; usually they are physically pulsating, expanding and contracting.

The most common way that stars are represented graphically is through the Hertzsprung-Russell diagram (see Figure 1.3). This is a plot of stellar luminosity vs.

temperature. The y-axis is often expressed in units of either Solar luminosities or magnitudes and is inverted. The x-axis of the H-R diagram is usually in terms of temperature, color, or spectral type, and is also inverted.

Spectral types correspond with stellar temperatures; O is hottest and M is coolest. Each of these is subdivided into ten types, labeled 0-9. Spectral types are assigned according to the Harvard spectral classification system, which began as a way of classifying the spectra according to the strengths of the hydrogen Balmer absorption lines in the spectra. A list of spectral types is given in Table 1.1.

When a large number of stars is plotted on the H-R diagram, several trends are seen. The largest of these, running through the middle of the plot, is called the Hydrogen Main Sequence. Stars located on this trend are doing the same thing as the Sun, fusing hydrogen into helium in their cores. They are more or less in hydrostatic equilibrium: maintaining the balance between the inward pull of gravity and the outward push of the radiation pressure generated by the reactions going on in their cores. Other groups can be seen in the H-R diagram in Figure 1.3, such as red giants and white dwarfs. These are stars in different evolutionary stages. The H-R diagram, therefore, shows stars in different stages of their life cycles. Another trend shown in Figure 1.3 is the Instability Strip, which extends down past the Main Sequence to the White Dwarf region. The Instability Strip contains variable stars; these are struggling to maintain hydrostatic equilibrium. δ Scuti stars are located in the section of the Instability Strip just above and touching the Hydrogen Main Sequence, so they are at the end of–or a little past–the hydrogen-fusing part of their evolution.

The light output of variable stars is generally represented by a light curve, which shows the light output over time. The light output is usually given in units of magnitudes, or differential magnitudes. Differential magnitudes compare the brightness of the star in question with the average brightness of the stars surrounding it. The time in a light curve plot is often shown in units of Heliocentric Julian Date (HJD). HJD is a standard time-keeping system used by astronomers. It corrects for the light travel time to the Sun at various points in Earth's orbit. When a star is
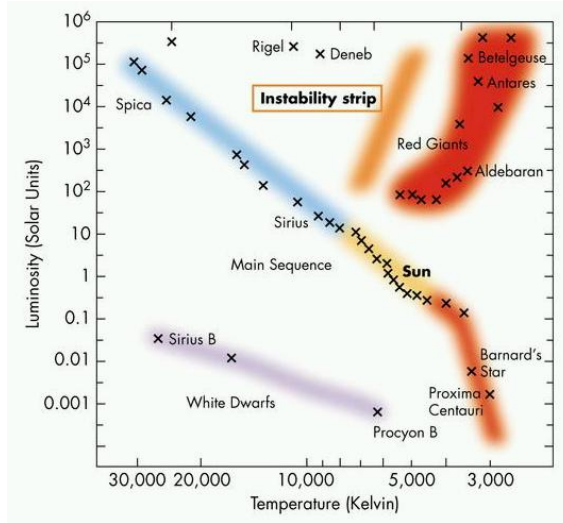
Figure 1.3: Hertzsprung-Russell diagram. Image from www.astro.umass.edu

Table 1.1.   Stellar Spectral Types

Spectral Type	Color	Surface Temp. (K)
O	Blue	30,000 to 60,000
B	Blue-White	10,000 to 30,000
A	White	7,500 to 10,000
F	Yellow-White	6,000 to 7,500
G	Yellow	5,000 to 6,000
K	Yellow-Orange	3,500 to 5,000
M	Red	under 3,500
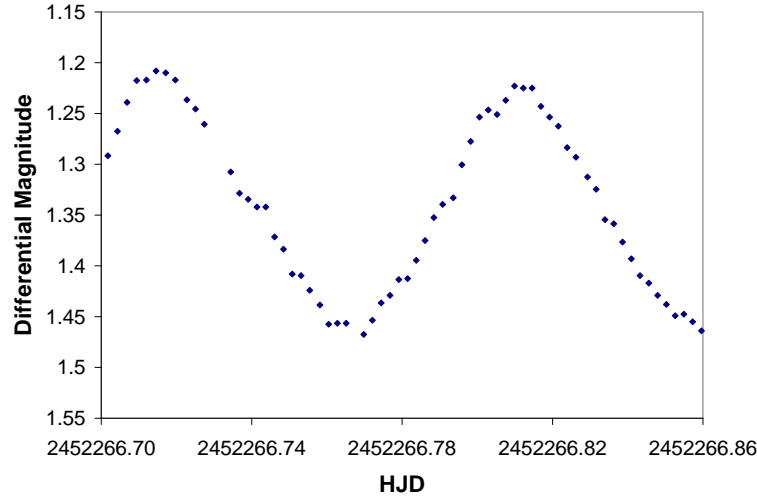
Figure 1.4: Light curve of δ Scuti star BO Lyncis. Data acquired at Orson Pratt Observatory on December 23, 2001 and reduced by author.

observed, the amount of time it takes for the light to reach Earth will vary depending on the location of Earth in its orbit around the Sun. HJD takes into account the difference in the time it takes the light to travel between the Earth and the Sun. Delta Scuti stars have relatively short pulsation periods, ranging from about 20 minutes to about five hours. Their spectral types range from about A0 to F5. The amplitude of δ Scuti light curves vary from 0.003 to about 0.9 mag. The light curve of a δ Scuti typically has a slightly faster rise than decline, as shown in Figure 1.4. Most δ Scutis are located in the disk of the Galaxy.

1.3   Telescope Systems

The only aspect of stars that is directly observable by astronomers is light output. Surprisingly, information about several stellar characteristics can be gleaned by studying this light output from these distant objects.

6
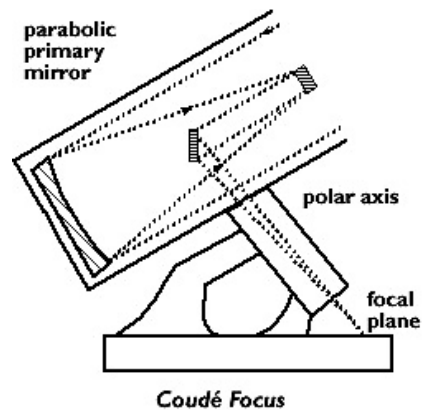
Figure 1.5: Coudé telescope focus. Image from www.as.utexas.edu

Telescopes are used to collect the light output from stars. A telescope gathers light and brings it to a focus so it can be studied. The two main types of telescopes are reflectors and refractors. Refractors use lenses to bend incoming light to a focus, while reflectors use mirrors. Reflecting telescopes are most common because of their advantages over refracting telescopes: they are cheaper to manufacture and result in less distortion of stellar images. The telescope used in this study is a reflecting telescope with a Coudé focus. As shown in Figure 1.5, the Coudé focus uses a primary mirror to reflect the incoming light back to a secondary mirror. The light is bounced back where it hits a third mirror that directs the light out the side of the telescope to the focal point, usually down the polar axis.

Focus configurations determine the length of the light path from the point it enters the telescope until it reaches the detector. This length is called the focal length. Different types of instruments and detectors can be put at the focal point, depending on the type of study being done. The instrumentation specifics used in this study are given in Chapter 2.
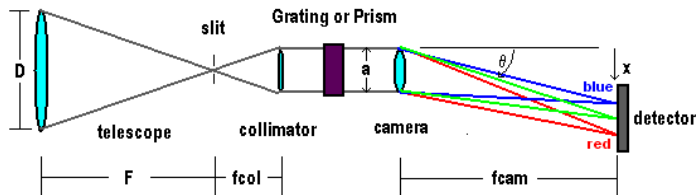
Figure 1.6: Basic spectrograph. Image from www.astro.ufl.edu

1.4 Spectroscopy

Spectroscopy is a branch of observational astronomy that entails studying a star's light output broken down into component wavelengths. The most basic instrument used in spectroscopy is a spectrograph. Figure 1.6 shows a basic spectrograph connected to a telescope. The slit of the spectrograph is situated at the focus of the telescope, at the image plane. The spectrograph uses a dispersion element, such as a prism or diffraction grating, to split the incoming light into its component wavelengths. A diffraction grating is a piece of glass that has closely spaced parallel grooves cut into it. The grating splits light into component wavelengths like a prism. Blazing is used in order to control the cross-sectional profile of the grooves on the grating. It concentrates most of the diffracted energy in a specific order at a particular wavelength. A diffraction grating can be blazed at a certain wavelength in order to provide maximum efficiency at that wavelength. A detector is placed at the end so that it can record the dispersed light at various wavelengths. Figure 1.7 gives two examples of how spectra are represented by the detector.

For this spectroscopic study, a charge-coupled device (CCD) was used as a detector for the spectrograph. A CCD is a detector in a camera that, in this case, takes a picture of the spectrum of the star being observed. A CCD is an array of pixels that count photons incident on them. Each pixel on a CCD can be thought of as an electron well. When photons hit a CCD, they trigger electrons that collect in
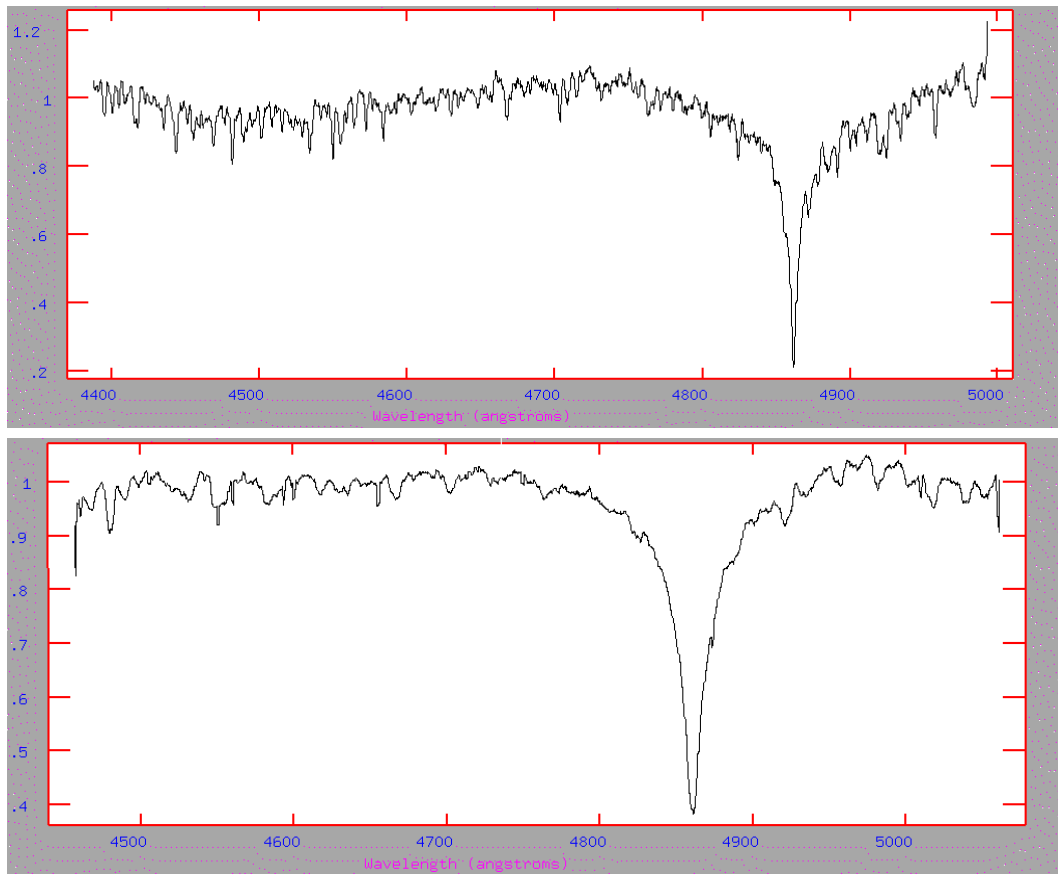
Figure 1.7: A spectrum of DK Virginis obtained on 6 Jun 2002 (*top*). A spectrum of FP Serpentis obtained on 6 March 2002 (*bottom*).
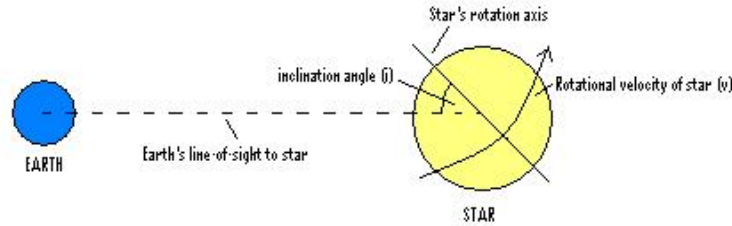
Figure 1.8: Projected rotational velocity.

the wells. The count of the electrons in the wells determines the observed magnitude of the incoming light.

1.5   Projected Rotational Velocity

Rotational velocity is a fundamental characteristic of stars that can be measured. The value calculated for a star's rotational velocity is actually a projected rotational velocity, $v \sin i$. There is usually no known method for determining the inclination of a star's rotational axis, so only $v \sin i$ can be calculated from Earth, where v is the actual rotational velocity of the star, and i is the axial inclination along Earth's line-of-sight, as shown in Figure 1.8.

When a star is rotating, one side is moving away from Earth and the other side is moving toward Earth. Therefore, the light from one side of the star is redshifted, while the light from the other side appears blueshifted (Figure 1.9). In this way, a star's rotation broadens its spectral lines. This concept was first suggested by Abney (1877). Spectral broadening can be seen in the absorption lines in the spectrum in Figure 1.7. The first example, DK Vir, is reported by Rodriguez et al. (2000) to have a $v \sin i$ value of 75 km/s, while FP Ser has a $v \sin i$ value of 210 km/s. The spectral features of FP Ser are broader due greatly to rotation. There are many known stars for which projected rotational velocity values have not yet been calculated. For the values that have been calculated, a few different methods have been used to measure and analyze the rotational broadening of the stars' spectral lines.
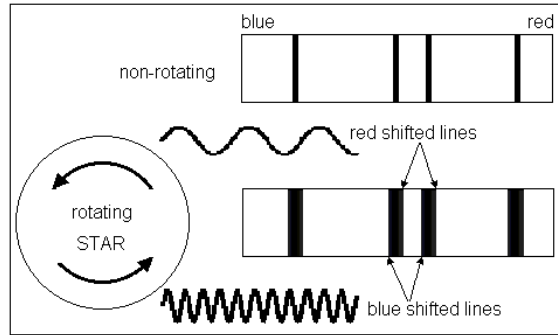
Figure 1.9: Rotational broadening. Image from http://hsc.csu.edu.au

Shajn & Struve (1929) suggested six influences on the widths of and intensity distributions in stellar spectral lines:

1. Disturbing effects of neighboring atoms which interfere with the quantum states of the absorbing atom;

2. Doppler effect due to the temperature motion of the particles (microturbulence);

3. Doppler effect due to ascending and descending currents of matter (convection);

4. Doppler effect due to rotation;

5. Compton scattering; and

6. Rayleigh scattering.

Equation 1.1, for the wavelength distribution of intensity in a spectral line, was produced to take all of the above factors into account.

$$I = F(\lambda) = I_0 \exp\left[-\kappa^2(\lambda - \lambda_0)^2\right] \qquad (1.1)$$

In Equation 1.1, I_0 is central intensity and λ_0 is central wavelength of the spectral line. For rotating stars, Equation 1.1 was integrated over the whole disk of the star. For a wavelength, the middle of the spectral feature was given by Equation 1.2:
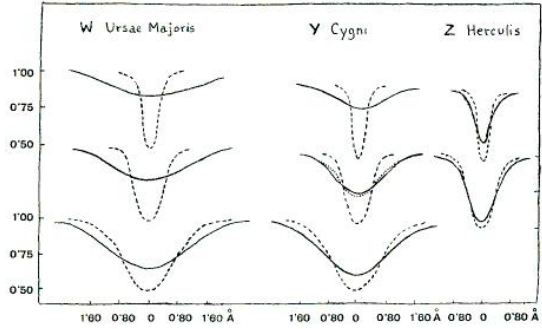
Figure 1.10: Theoretical stellar line profiles computed by Shajn & Struve (1929). The more broadened line profile is shown on the left, with the least broadened profile on the right.

$$\lambda_0' = \lambda_0 + \lambda_0(v/c) \tag{1.2}$$

In Equation 1.2, v is the radial component of the rotational velocity. Figure 1.10 shows the solutions computed for three different stars. This graphical method of Shajn & Struve (1929) has been used by other researchers since, as given below.

Struve (1930) found more rapidly rotating stars than were previously believed to have existed. B- and A-type stars were shown to be more likely to be fast rotators. The F spectral type showed fewer rapid rotators, and no cases of rapid rotation were found in single G-, K-, and M-type stars. Therefore, it appeared that rotational velocity is a function of spectral type, with the fastest rotations found in the earlier spectral types. Since then, rapid rotations have been found in later spectral types, and it has been thought by Dall et al. (2006) and others that the rapid rotations are the cause for strong magnetic activity found in some single late-type stars.

Struve (1930) examined the contours of stellar absorption lines and adapted the following list of factors that contribute to the observable broadening of stellar absorption contours:

1. Atomic abundance;

2. Molecular Stark effect; and

3. Stellar axial rotation.

The amount of atoms in the right state to absorb a particular wavelength of light depends on the star's temperature and pressure. It was found that this atomic abundance effect was negligible. The Stark effect, produced by electric fields of nearby ions, was also found to be negligible. Therefore, all broadening was assumed to be the result of rotation of the observed star. The rotational broadening measured in the line profiles was converted to $v \sin i$ values by comparing measured profiles to theoretical profiles computed through the graphical method of Shajn & Struve (1929).

Slettebak (1954) suggested that the fact that some types of stars rotate more rapidly than others is a clue to the puzzle of stellar evolution. In a series of investigations aimed at studying how the axial rotation of stars varies across the H-R diagram, Slettebak (1954 & 1955) and Slettebak & Howard (1955) determined $v \sin i$ values for 579 of the brighter stars, spanning spectral types B to G. Observed line profiles of different spectral features were compared to theoretical line profiles computed by the graphical method of Shajn & Struve (1929). Two independent line profiles of the same spectral feature were compared for each star, and the two resulting $v \sin i$ values were averaged together. For the types B2-B5, the HeI 4471 Å line was used. For types B8-A2, the MgII 4481.2 Å line was used. For types A3-G0, the MgII 4481.2 Å and the FeI 4071.8 Å lines were used. An earlier investigation by Stettebak (1949) used the same method with the HeI 4026 Å line for O, B, and Be stars. The investigation of Slettebak (1954) also lent support for the random distribution of stellar rotation axes. A plot of $v \sin i$ versus galactic position was made of the stars measured and showed no correlation.

Gray (1982, 1984, 1989) used Fourier analysis to find rotational velocities, studying the rotational broadening of the spectral lines of the stars. Spectra of stars were obtained and compared to spectra from model-atmosphere profiles. Fourier transforms of the actual spectral line profiles were divided by the Fourier transforms of the instrumental profiles, removing instrumental broadening. Model atmosphere

profiles were created for different spectral types. For each star, the Fourier transform of its actual line profile was convolved with the Fourier transform of its matching spectral type model profile. The model profiles were artificially broadened to model different rates of rotation. The actual profiles were compared in this way to the model profiles in order to find the best match. The matching of the profiles resulted in reported rotational velocity values for the observed stars.

Fekel (1997, 2003) developed a method of calibrating spectral line profile broadening with known rotational velocity values. High-dispersion spectroscopic observations were obtained by Fekel (1997), centered at 6430 Å, with a wavelength range of 80 Å. The full width at half-maximum (FWHM) values for several moderate strength spectral lines were measured and averaged together. The FWHM values for several comparison arc lines were also measured and averaged together. This arc broadening was assumed to be the instrumental broadening for the spectral features. The instrumental broadening was removed by taking the square root of the difference of the squares of the two measurements, and the result was assumed to be the intrinsic stellar line broadening due to both rotation and macroturbulence. The $v \sin i$ values from Gray (1982, 1984, 1989) were used to convert the stellar broadening from each star into a $v \sin i$ value. To calibrate the results, the mean FWHM values for the stars were plotted against Gray's $v \sin i$ values for the 57 stars common to the Fekel (1997) and the Gray (1982, 1984, 1989) data sets. The calibration curve was calculated from a second-order polynomial, given by Equation 1.3.

$$FWHM_{intrinsic} = 0.04082 + 0.02509X + 0.00014X^2 \qquad (1.3)$$

In Equation 1.3, X is the value of Gray's total broadening. This calibration equation was used to convert the mean FWHM in angstroms into a total line broadening in km/s. Macroturbulent broadening was also removed. A mean value for macroturbulence over each spectral range was assigned, which was assumed to be a good representation for most stars. A macroturbulence of 5 km/s was assumed for

early-F dwarfs (Gray 1982a) and 5-3 km/s for F-K subgiants (Gray and Nagar 1985). Macroturbulence was then removed from the total broadening by taking the square of the difference of the squares of the two values (total broadening value and macro-turbulence value), resulting in the assumed $v \sin i$ values. For stars having more than one observation, average $v \sin i$ values were determined.

Fekel (2003) built on this method to calculate projected rotational velocity values for stars with spectra in another wavelength region. This time spectra were taken in two wavelength ranges, one centered again at 6430 Å and one centered at 4500 Å. Once more, the wavelength range was 80 Å. From mid-B to early-F spectral types, Fe II and Ti II FWHM values were obtained in the 4500 Å region. The FWHM values were again averaged and instrumental broadening was removed the same way as before. A new second-order polynomial was used to calibrate the data in the 4500 Å region (Equation 1.4):

$$FWHM_{4500} = 0.08016 + 0.01284X + 0.00011X^2 \qquad (1.4)$$

In Equation 1.4, X is the value of the total intrinsic broadening found in the 6430 Å region. This calibration curve was fit to the 4500 Å region data. In the same way as Fekel (1997), a 5 km/s macroturbulence was removed for early-F stars. No macroturbulent broadening was removed for B and A stars. An uncertainty of 1 km/s was assumed for $v \sin i$ values near 20 km/s and an uncertainty of 3 km/s was assumed for values near 50 km/s. An average $v \sin i$ value was found for stars with more than one observation.

Royer (2002a,b) put together a catalog of rotational velocity values for B8-F2 spectral type stars from one internally consistent data set. Royer et al. (2002a) calculated velocities for 525 stars in the southern hemisphere, while Royer et al. (2002b) calculated velocities for 249 stars in the northern hemisphere. A Fourier transform method was used to calculate rotational velocities that differed slightly from the method used by Gray (1982, 1984, 1989). The method adopted was suggested

first by Carroll (1933). Instead of comparing the Fourier transform of the entire observed line profiles, only the Fourier transforms of the zeros of the profiles were used. It was thought by Carroll (1933) that examining the first lobe of the Fourier transform gave a better indication of the rotational broadening of the spectral feature. A Fourier transform of the 4350 Å spectral feature was computed. The first zero of the transform was compared to that of a Fourier transform of a model feature at the same wavelength. The model was artificially broadened for rotation, and the profiles were matched for the best rotational broadening fit.

1.6 Hydrogen-Beta Color Index

Color indices are usually obtained photometrically, but they can also be measured using spectra. The Planck curves (spectral energy curves) for different stars peak at different wavelengths, because different stars have different temperatures (Figure 1.11). Hotter stars are bluer, and cooler stars are more red. Therefore, a star's temperature can be measured through its color index. A color index is the difference between a star's photometric magnitudes measured over two different effective wavelength regions. In Equation 1.5, m is the magnitude of the respective wavelengths, λ.

$$CI = m(\lambda_1) - m(\lambda_2) \tag{1.5}$$

The long-wavelength magnitude is subtracted from the short-wavelength magnitude. There are several different color indices. For example, a (B-V) color index gives the difference between the blue magnitude and the visual magnitude of a star. Color index is equivalent to the flux ratio of the wavelengths being used, as shown in Equation 1.6.

$$CI = constant - 2.5 \log \left[F(\lambda_1)/F(\lambda_2) \right] \tag{1.6}$$
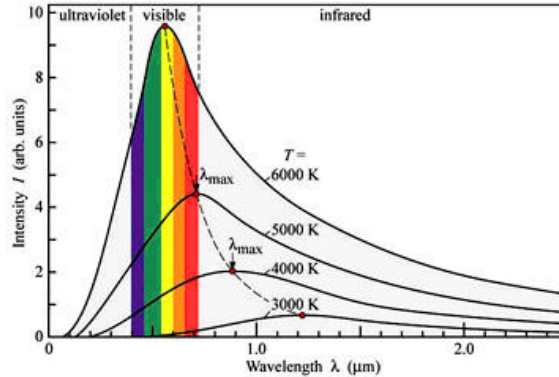
Figure 1.11: Planck curves. Image from www4.nau.edu

The constant in Equation 1.6 is the calibration constant for the system in question. $F(\lambda_1)$ and $F(\lambda_2)$ are the observed fluxes at the given wavelengths.

Color indices are calibrated so that they are instrument-dependent. The (B-V) color index of a star with a surface temperature of about 10,000 K, such as Vega, is zero. So in (B-V), a negative color index suggests a hotter star, and a positive color index is for a cooler star. The (B-V) color of a bluer star would be negative, because it is brighter in the blue than in the visible. A reddish star, on the other hand, would have a positive (B-V) color index, because it is brighter in the visual than in the blue. Different color indices are useful for measuring temperatures of different stars.

Interstellar reddening is an obstacle that is faced by astronomers using color indices. Blue light is more easily scattered by interstellar dust grains than red light, making reddening wavelength dependent. It affects magnitudes at different wavelengths unequally. As a result, a single color index using only two different colors cannot always be used to determine the temperature of a star; three or more different color magnitude measurements are often necessary (Zeilik & Gregory (1998)).

The Hydrogen-β (Hβ) color index has the advantage of being reddening free. This is because both filters used in the index are centered on the same effective wavelength: the Hβ line at 4861 Å. Crawford & Mander (1966) standardized the Hβ system through photometric observations of 80 stars. In the Hβ system, two filters

17
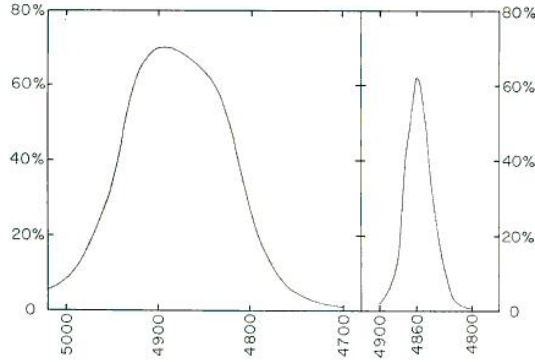
Figure 1.12: Transmission curves for Hβ filters Crawford & Mander (1966).

are used: a wide and a narrow filter. The narrow filter has a half-width of about 30 Å and the wide filter has a half-width of about 150 Å. Observations are taken of each star using each filter. The resulting color index follows Equation 1.7, where $F(\beta_W)$ is the flux of the star through the wide filter, and $F(\beta_N)$ is the flux of the star through the narrow filter.

$$H\beta = -2.5 \log\left[F(\beta_W)/F(\beta_N)\right] \tag{1.7}$$

Equation 1.8 shows this relation in magnitudes.

$$H\beta = m(\beta_N) - m(\beta_W) \tag{1.8}$$

The flux through each filter is found using the transmission curve of the filter. Figure 1.12 shows the transmission curves for two filters used by Crawford & Mander (1966). The transmission curves show how much light is transmitted through the filter at which wavelengths. The acquired spectrum, including the Hβ line profile, is multiplied by the transmission curve, and the result is integrated across all wavelengths, as given in Equation 1.9.

$$F(\beta_W) = \int S(\lambda)T(\lambda)d\lambda \qquad (1.9)$$

In Equation 1.9, $S(\lambda)$ is the spectral line profile, and $T(\lambda)$ is the transmission curve, both as a function of wavelength.

1.7 Project Scope

During several observing runs at the Dominion Astrophysical Observatory, spectroscopic observations were made of the δ Scuti stars in the Rodriguez et al. (2000) catalog brighter than 13th magnitude and north of -01 degrees declination for a radial velocity study at Brigham Young University. The Hydrogen-β region of the stellar spectra were measured, with a dispersion that included several weak metal lines. There are several δ Scuti stars in the data set that have no previously published rotational velocity values. In this project, a method was developed for calculating the rotational velocities of those stars. The stars brighter than 7th magnitude were used in developing the method. The observations of these brighter stars had a better signal-to-noise ratio than the others, and they comprised over half of the data set. There is a considerably higher percentage of stars 7th magnitude and dimmer with missing rotational velocity values. The method was developed so that it can be used in the future to find values for the dimmer stars in the data set. Rotational velocity values for four stars with previously unknown values were calculated with the method developed. Since the spectra were taken of the Hβ region, they naturally lend themselves to an analysis of Hβ color index as well. A method for finding the Hβ color index values for the stars in the data set was similarly developed. Hβ color index values were found for five stars with previously unknown values.

Chapter 2

Procedures and Methods

2.1 Spectroscopic Observations

Spectroscopic observations were secured at the Dominion Astrophysical Observatory in eight observing runs during 2002 and 2003. The 1.2-m McKellar Telescope was used to acquire these observations in the Hβ region. Observations were taken with the spectrograph mounted at the Coudé focus using the 32121 grating. The grating is blazed at 5000 Å and yields 10.1 Å/mm. The SITe4 CCD was used, which has 15 micron pixels. Tables 2.1 through 2.4 show the observed stars, broken down into magnitude ranges. Observations were taken on 167 of the 233 northern hemisphere δ Scuti stars from the Rodriguez et al. (2000) catalog brighter than 13th magnitude, one of which is a rotational velocity standard, as found in Slettebak et al. (1975). An additional rotational velocity standard star that is not a δ Scuti was also observed. Table 2.5 lists the central wavelength and coverage of the reflection grating, as well as the plate scale of the CCD-spectrograph system for each reduced observing run.

Image exposure times ranged from 8 to 800 seconds, depending on the visual magnitude of the star and sky conditions. Typically, about 20 bias frames and about 15 flat field frames were taken each night. Arc frames were typically taken sandwiching the image frames, with one on each side of each object frame. The telescope had the same position and orientation for the sandwiching arc frames as it had for the object frames. This way the arc frames are taken close to the observation time of the object, and hopefully there would be minimal, if any, system variations between these measurements due to instrument orientation.

Table 2.1.   Spectroscopic Observations of δ Scutis Brighter Than 7th Magnitude

Star	V mag	Observing Run	# Obs.	Star	V mag	Observing Run	# Obs.
41 Peg	6.33	Aug 2002	3	V340 And	5.55	Aug 2002	3
AI CVn	6.03	Mar 2002	25	V352 Aur	6.16	Feb 2003	2
AO CVn	4.72	Jun 2002	3	V376 Per	5.95	Feb 2003	3
AZ CMi	6.46	Feb 2003	4	V377 Cep	6.61	Aug 2002	2
BT Cnc	6.65	Feb 2003	2	V386 Per	6.54	Feb 2003	3
CL Dra	4.96	Jun 2002	4	V388 Cep	5.56	Aug 2002	2
CN Boo	5.98	Jun 2002	2	V480 Tau	5.08	Feb 2003	2
CN Dra	6.34	Jun/Aug 2002	6	V483 Tau	5.58	Feb 2003	3
CO Lyn	6.83	Mar 2002	5	V509 Per	6.48	Feb 2003	3
CX Cnc	6.05	Feb 2003	3	V521 Per	6.38	Feb 2003	3
CX UMa	6.93	Mar 2002/Feb 2003	2	V526 Cas	6.38	Aug 2002	5
DD UMa	4.80	Feb 2003	3	V620 Her	6.20	Jun/Aug 2002	5
DK Vir	6.69	Jun 2002	1	V644 Her	6.35	Jun 2002	4
DP UMa	5.22	Jun 2002	4	V696 Tau	5.26	Feb 2003	1
EM Aqr	6.55	Aug 2002	3	V775 Tau	5.72	Feb 2003	3
EN UMa	5.88	Mar 2002	2	V777 Tau	4.48	Feb 2003	3
EP Cnc	6.77	Feb 2003	3	V784 Cas	6.66	Feb 2003	3
ER Dra	6.26	Jun 2002	1	V831 Her	6.34	Jun/Aug 2002	6
FI UMa	6.63	Feb 2003	4	V1004 Ori	5.89	Feb 2003	3
FM Com	6.46	Jun 2002	3	V1208 Aql	5.53	Jun/Aug 2002	6
FM Vir	5.22	Jun 2002	3	V1276 Cyg	6.54	Jun/Aug 2002	5
FP Ser	6.28	Mar 2002	3	V1431 Aql	5.79	Jun 2002	2
FQ Boo	6.60	Mar 2002	3	V1644 Cyg	4.93	Jun/Aug 2002	19
GG Vir	6.22	Jun 2002	2	V2112 Oph	6.51	Jun/Aug 2002	6
GN And	5.20	Aug 2002	3	VV Ari	6.70	Aug 2002	2
GX Peg	6.33	Aug 2002	5	VW Ari	6.70	Aug 2002	5
HT Peg	5.30	Aug 2002	7	VX Psc	6.01	Aug 2002	6
II Vir	6.52	Mar 2002	1	VY Psc	6.55	Aug 2002	3
IK Peg	6.08	Aug 2002	3	XX Psc	6.11	Aug 2002	3
IM Tau	5.39	Feb 2003	3	β Cas *	2.28	Aug 2002	3
IQ Vir	6.31	Jun 2002	3	β Vir **	3.61	Mar 2002	4
KW 284	6.76	Feb 2003	3	γ Boo	3.04	Jun 2002	3
KW Aur	5.01	Mar 2002	3	δ Del	4.43	Aug 2002	3
LT Vul	6.61	Jun/Aug 2002	6	δ Ser	3.80	Aug 2002	2
NU Vul	5.19	Jun/Aug 2002	6	ϵ Cep	4.18	Aug 2002	3
OX Aur	6.10	Feb 2003	2	$\theta2$ Tau	3.40	Feb 2003	3
RX Sex	6.68	Mar 2002	2	ι Boo	4.75	Jun 2002	3
SAO 52892	6.51	Aug 2002	3	$\kappa2$ Boo	4.53	Mar 2002	3
SAO 72399	6.54	Aug 2002	3	λ Boo	4.18	Jun 2002	3
SAO 88295	5.51	Aug 2002	2	ν UMa	3.78	Feb 2003	6
SAO 141427	6.25	Jun 2002	4	ρ Tau	4.65	Feb 2003	3
SAO 143373	6.50	Aug 2002	4	τ Peg	4.58	Aug 2002	2
UU Ari	6.14	Feb 2003	2	υ Tau	4.28	Feb 2003	3
UV Ari	5.17	Feb 2003	3				

* Rotational velocity standard, δ Scuti

** Rotational velocity standard, not δ Scuti

Table 2.2.   Spectroscopic Observations of δ Scutis from 7th to 8th Magnitude

Star	V Mag	Observing Run	# Obs.	Star	V Mag	Observing Run	# Obs.
AD Ari	7.43	Aug 2002	3	V1745 Cyg	7.44	Jun 2002	3
AR Ari	7.82	Feb 2003	2	V2084 Cyg	7.35	Jun 2002	3
BH Psc	7.12	Aug 2002	3	V2109 Cyg	7.51	Jun 2002	3
BN Cnc	7.8	Feb 2003	2	V2109 Cyg	7.51	Aug 2002	21
BU Cnc	7.67	Feb 2003	3	V2314 Oph	7.43	Jun 2002	3
BX Cnc	7.96	Feb 2003	3	V2314 Oph	7.43	Aug 2002	3
BY Cnc	7.9	Feb 2003	3	V345 Gem	7.78	Mar 2002	3
CQ Lyn	7.97	Feb 2002	35	V350 Peg	7.2	Aug 2002	3
		Mar 2003	4			Sep 2003	6
CR Lyn	7.65	Mar 2002	5	V361 And	7.71	Aug 2002	3
DL UMa	7.2	Mar 2002	3	V365 And	7.42	Aug 2002	3
DQ Cep	7.26	Jun 2002	2	V373 And	7.58	Aug 2002	3
		Aug 2002	2	V377 Cas	7.83	Aug 2002	2
DR Psc	7.23	Aug 2002	3			Sep 2003	3
DX Cet	7	Aug 2002	2	V383 Vul	7.17	Jun 2002	4
EE Cam	7.71	Mar 2002	4			Aug 2002	3
EO UMa	7.12	Mar 2002	3	V396 And	7.86	Aug 2002	3
		Feb 2003	35	V456 Aur	7.83	Mar 2002	7
FL Cnc	7.03	Mar 2002	3	V459 Cep	7.65	Aug 2002	3
HIP 59015	7.54	Mar 2002	6	V479 Tau	7.44	Feb 2003	3
		Feb 2003	17	V544 Lyr	7.45	Jun 2002	3
HQ UMa	7.11	Mar 2002	3			Sep 2003	3
IP UMa	7.66	Jun 2002	4	V579 Per	7.84	Feb 2003	3
		Feb 2003	32	V650 Tau	7.76	Feb 2003	3
KW 385	7.92	Feb 2003	4	V764 Mon	7.16	Mar 2002	3
NN Peg	7.25	Aug 2002	3	V929 Her	7.99	Jun 2002	3
NT Hya	7.37	Mar 2002	6	V966 Her	7.98	Mar 2002	3
PV Gem	7.52	Mar 2002	3			Aug 2002	2
SAO 16394	7.53	Jun 2002	3			Feb 2003	18
SAO 43050	7.79	Feb 2003	3			Sep 2003	6
SAO 74848	7.89	Aug 2002	4	VZ Cnc	7.73	Mar 2002	10
SAO 107656	7.56	Aug 2002	3				
SAO 140074	7.84	Jun 2002	2				
V1438 Aql	7.72	Jun 2002	2				
		Aug 2002	9				
		Sep 2003	1				

Table 2.3.   Spectroscopic Observations of δ Scutis from 8th to 9th Magnitude

Star	V Mag	Observing Run	# Obs.
EI Dra	8.54	Jun 2002	3
GG UMa	8.66	Mar 2002	3
GS UMa	8.68	Mar 2002	1
IN Dra	8.02	Aug 2002	3
QS Gem	8.84	Mar 2002	3
SAO 22973	8.56	Feb 2003	3
SAO 43060	8.14	Feb 2003	2
SAO 55300	8.78	Aug 2002	1
SAO 75119	8.25	Aug 2002	2
TU UMi	8.77	Jun 2002	2
V360 Cep	8.52	Aug 2002	3
V549 Lyr	8.06	Jun 2002	3
		Sep 2003	3
V873 Her	8.39	Jun 2002	3
		Feb 2003	12
		Sep 2003	2
V919 Her	8.36	Jun 2002	3
V979 Her	8.48	Jun 2002	3
V1719 Cyg	8.01	Aug 2002	19
V2129 Cyg	8.32	Aug 2002	2
V2088 Cyg	8.24	Jun 2002	2

Table 2.4.   Spectroscopic Observations of δ Scutis from 9th to 13th Magnitude

Star	V Mag	Observing Run	# Obs.
GW Dra	9.31	Mar 2002	6
		Feb 2003	4
GW UMa	9.6	Mar 2002	2
		Feb 2003	6
V1003 Her	9.76	Aug 2002	1
		Feb 2003	2
V336 Sge	9.3	Aug 2002	1
V830 Her	9.3	Jun 2002	2
AN Lyn	10.66	Feb 2003	6
V577 Oph	10.8	Feb 2003	3
V927 Her	10.08	Feb 2003	6
CW Ser	11.98	Feb 2003	6
V567 Oph	11.08	Feb 2003	4
V959 Oph	11.4	Feb 2003	2
BO Lyn	12	Feb 2003	12

Table 2.5.   CCD-Spectrograph Specifics

Observing Run	Central Wavelength (Å)	Coverage (Å)	Plate Scale (Å/Pixel)
March 2002	4825	4500 to 5150	0.163
June 2002	4700	4400 to 5000	0.150
August 2002	4700	4400 to 5000	0.150
February 2003	4800	4400 to 5000	0.175

2.2   Image Reductions

All of the 87 stars brighter than 7th magnitude, listed in Table 2.1, were reduced using standard spectral reduction packages in the Image Reduction and Analysis Facility (IRAF). This group of stars is over half of the data set, and was reduced for use in developing analysis methods for the rest of the set. Reducing frames basically involves image processing that converts raw data frames into a format that is suitable for analysis. One step in this process entails applying the acquired calibration frames to the image frames. Figure 2.1 shows examples of unprocessed calibration and image frames. Each pixel on a CCD responds differently to light. Also, the electronics of the telescope–CCD system affect the measurements. The calibration frames are applied to the image frames to correct for these effects. This section gives the process by which data reductions were carried out in this study. More detail is given where processing differs from photometric reductions, since few complete spectral reductions are described in past theses from Brigham Young University.

2.2.1   Updating Headers and Trimming Frames

The image and calibration frames have headers in their files that need to contain certain information for different data reduction packages. Some examples of information found in a header file are image name, exposure time, filter(s) used, observation date and time, and observer. If the image frames have been processed, the header file will also reflect that. Figure 2.2 gives an example of a header for the
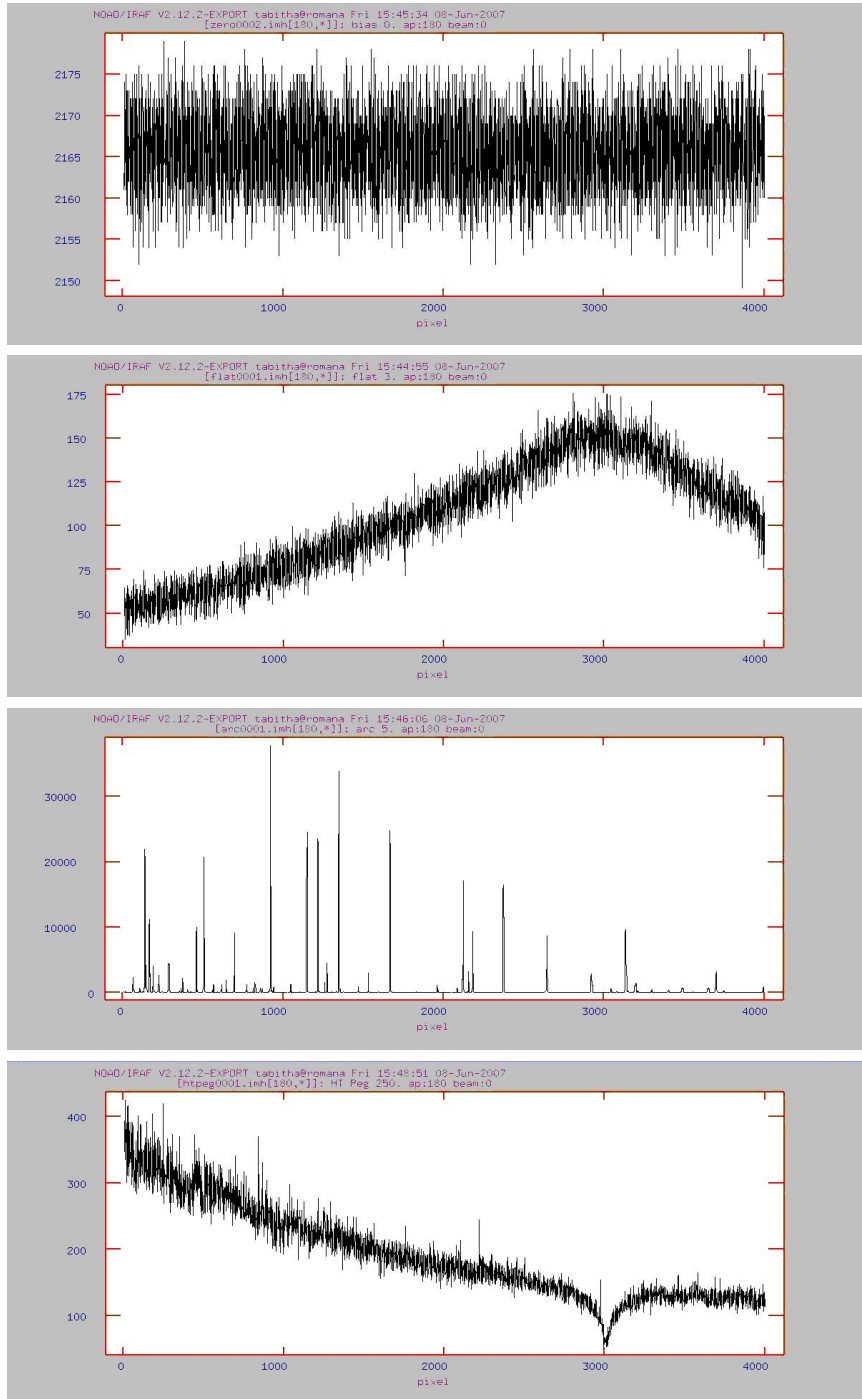
Figure 2.1: Unprocessed bias frame (*top*), flat field frame (*second*), FeAr arc frame (*third*), and object frame (HT Pegasi) (*bottom*).

```
taupegcr0001.imh[360,3991][real]: tau Peg
No bad pixels, min=unknown, max=unknown
Line storage mode, physdim [384,3991], length of user area 1904 s.u.
Created Tue 00:11:12 27-Mar-2007, Last modified Tue 00:11:16 27-Mar-2007
Pixel file "romana!/home/iraf/images/tabitha/taupegcr0001.pix" [ok]
'DAO'                  /
New copy of taupeg0001.imh
New copy of taupeg0001.imh
New copy of taupeg0001.imh
EXPTIME =                200 /
INSTRUME= 'SITe-4'          /
XBIN    =                  1 /
YBIN    =                  1 /
PIXSIZE =                 15 / pixel size, microns
CTYPE1  = 'PIXEL   '          /15 / axis1 in pixels
CTYPE2  = 'PIXEL   '          /15 / axis2 in pixels
CCDTEM  =              -59.0 /
DATE-OBS= '2002-08-11T09:59:17'/
RA      = '23:21:03.52'        /  AT START OF EXPOSURE
DEC     = '23:46:24.90'        /  AT START OF EXPOSURE
EPOCH   = '2002.63         ' / OF RA and DEC AT START OF EXPOSURE
SIDEREAL= '23:04:27.72     ' / AT START OF EXPOSURE
HA      = '-00:16:36.80    ' / AT START OF EXPOSURE
OBSTYPE = 'object          ' / OBSERVATION TYPE
OBSERVER= 'Hintz'
IMAGETYP= 'object  '
DISPAXIS= '2      '
RDNOISE = '7      '
GAIN    = '1.8    '
OBSERVAT= 'dao    '
OBS     = '@observat'
ST      =      23.0743666666667
AIRMASS =           1.102531
UTMIDDLE= '10:01:40.0'
JD      =      2452497.91732639
HJD     =      2452497.92121065
LJD     =            2452497.
WCSDIM  =                  2
CDELT1  =                 1.
CDELT2  =                 1.
CD1_1   =                 1.
CD2_2   =                 1.
LTM1_1  =                 1.
LTM2_2  =                 1.
WAT0_001= 'system=image'
WAT1_001= 'label=pixel'
WAT2_001= 'label=pixel'
TRIM    = 'Mar 26 23:56 Trim data section is [1:360,10:4000]'
CCDSEC  = '[1:360,10:4000]'
CRPIX2  =                 -9.
LTV2    =                 -9.
CCDPROC = 'Mar 27  0:04 CCD processing done'
ZEROCOR = 'Mar 27  0:04 Zero level correction image is Zero.imh'
FLATCOR = 'Mar 27  0:04 Flat field image is nFlat.imh with scale=1.'
CRCOR   = 'Threshold= 25.0, fluxratio=  2.00, removed=1359'
REFSPEC1= '_arc0020 '
```

Figure 2.2: Example of image header file for τ Pegasi.

star τ Pegasi. There is no standard formatting system for observatories to use when structuring header files, so sometimes information needs to be added later.

The HJD and the airmass for each observation needed to be added to the header files for IRAF reduction purposes (HJD was explained in Section 1.2). The airmass value corresponds to the amount of Earth's atmosphere through which the light from a star must travel in order to reach the telescope. Ninety degrees from the horizon (at the zenith) the airmass is at a value of unity, and 30 degrees above the horizon corresponds to an airmass of two. Between these two points, a relation is

```
title            "V1431 Aql"
imagetyp         "object"
observat         "dao"
dispaxis         "2"
ut sexstr        (@'DATE-OBS')
obs              @"observat"
rdnoise          "7"
gain             "1.8"
st               @"sidereal"
```

Figure 2.3: Example of *.cmds* file for V1431 Aquilae.

used to calculate airmass. Other header information was updated using *.cmds* files. Figure 2.3 gives an example of a *.cmds* file for V1431 Aquilae.

CCDs sometimes have bad columns on them that impact the data taken. The bad columns on the SITe-4 CCD at DAO are fortunately on the edge of the chip. The first ten columns of all data frames were therefore trimmed off using the IRAF command *ccdproc*.

2.2.2   Processing Bias Frames

A bias frame shows the pixel response across the CCD to the electronics of the CCD imaging and readout system. It is a zero-second exposure, taken with the shutter closed. Several bias frames are taken and averaged together, and the combined bias frame is then subtracted from the image frames. This process is done the same way as in photometric reductions. The IRAF command *zerocombine* is used to combine the bias frames into one master bias frame, and the IRAF command *ccdproc* is used to subtract the bias master from the flat field frames. Figure 2.4 shows the different parameters found in *ccdproc*.

```
PACKAGE = ccdred
   TASK = ccdproc

images  =          arc*.imh  List of CCD images to correct
(output =                 )  List of output CCD images
(ccdtype=             comp)  CCD image type to correct
(max_cac=                0)  Maximum image caching memory (in Mbytes)
(noproc =               no)  List processing steps only?

(fixpix =               no)  Fix bad CCD lines and columns?
(oversca=               no)  Apply overscan strip correction?
(trim   =               no)  Trim the image?
(zerocor=               no)  Apply zero level correction?
(darkcor=               no)  Apply dark count correction?
(flatcor=              yes)  Apply flat field correction?
(illumco=               no)  Apply illumination correction?
(fringec=               no)  Apply fringe correction?
(readcor=               no)  Convert zero level image to readout correction?
(scancor=               no)  Convert flat field image to scan correction?

(readaxi=             line)  Read out axis (column|line)
(fixfile=           badpix)  File describing the bad lines and columns
(biassec=                )  Overscan strip image section
(trimsec=   [1:360,10:4000]) Trim data section
(zero   =        Zero.imh)  Zero level calibration image
(dark   =        Dark.imh)  Dark count calibration image
(flat   =       nFlat.imh)  Flat field images
(illum  =                )  Illumination correction images
(fringe =                )  Fringe correction images
(minrepl=              1.)  Minimum flat field value
(scantyp=        shortscan)  Scan type (shortscan|longscan)
(nscan  =                1)  Number of short scan lines

(interac=               no)  Fit overscan interactively?
(functio=          legendre) Fitting function
(order  =                1)  Number of polynomial terms or spline pieces
(sample =                *)  Sample points to fit
(naverag=                1)  Number of sample points to combine
(niterat=                1)  Number of rejection iterations
(low_rej=               3.)  Low sigma rejection factor
(high_re=               3.)  High sigma rejection factor
(grow   =               0.)  Rejection growing radius
(mode   =               ql)
```

Figure 2.4: Parameters in *ccdproc*

2.2.3   Processing Flat Frames

Since each pixel on a CCD responds differently to light, flat frames are needed to measure this uneven pixel to pixel response. A flat frame is a calibration frame that is taken as the CCD is exposed to a flat field, or a field where the light is evenly distributed. If each pixel is exposed to the same amount of light, the brightness response can be measured. The mean of the flat field is computed and used to scale the flat. The image frames are then divided by this scaled flat. The IRAF task *flatcombine* is used to combine the flat field frames into one master flat frame, just as in photometric reductions. In spectroscopic data acquisition, a flat field frame is a two-dimensional spectrum of a lamp taken through the slit of the spectrograph, as shown in Figure 2.5. This results in a sharp dropoff in flat field signal on the CCD outside the aperture of the slit. Where there is no signal outside the aperture, there is still noise due to the instrumentation, and dividing the image frames by this

29
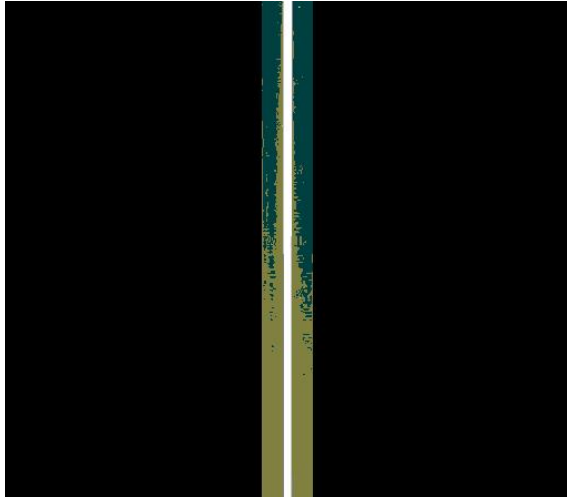
Figure 2.5: Slit aperture view of flat field frame

would remove part of the object profile. In order to divide the flat properly through the image frames, the IRAF task *apflatten* is used. The task *apflatten* models the profile and spectrum shape and removes them from the flat field. The user is asked by *apflatten* to define the aperture for the flat field. In this study the aperture was defined as shown in Figure 2.6. The spectrum inside the defined aperture is fit by a model profile that is divided into the flat field inside the aperture. Points outside the defined aperture are set to a value of unity. This results in a flat field that is properly scaled across the frame. The master flat frame is then applied to the image and arc frames using the flat correction parameters in the IRAF task *ccdproc*.

2.2.4 Removing Cosmic Rays

Any cosmic rays that may have been captured in an image during an object's exposure need to be removed before the object frames can be processed. The IRAF task *cosmicrays* is used to remove cosmic ray events from the image frames. A pixel detection window is set up on the image by the program, either 5x5 or 7x7 pixels. The flux of the brightest pixel in the detection window is compared to the mean flux of the surrounding pixels, excluding the second-brightest pixel in the window. If
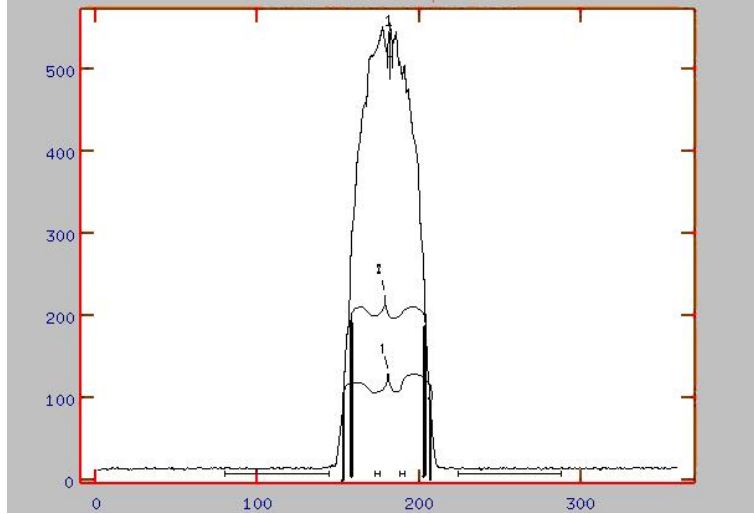
Figure 2.6: Defining the aperture for the flat field. A better signal to noise ratio was found by marking the aperture according to 2 than to 1, as shown.

the flux of the brightest pixel exceeds the mean flux of the neighboring pixels by a predetermined threshold value, the brightest pixel becomes a cosmic ray candidate. The flux of the candidate pixel is replaced by the mean flux of its four neighboring pixels. Figure 2.7 shows a spectrum of GN Andromedae with a cosmic ray and the image after the cosmic ray was removed. The *cosmicrays* task didn't always remove all of the cosmic rays from the spectra, as can be seen in Figure 2.7. Defects in the CCD chip also sometimes create artificial downward spikes in the spectra. These artificial features could be mistaken as actual spectral features by the IRAF routine that calculates color index. Therefore, before Hβ index analysis, these spikes were removed manually. Care was taken not to remove spectral features, and no spike wider than 5 pixels was removed.

2.2.5 Wavelength Calibration

In spectroscopy, images of spectra are taken which show the intensity of light over a range of wavelengths. These wavelengths correspond to different positions on the CCD, but they are often out of alignment with the pixels on the CCD. As a result,

31
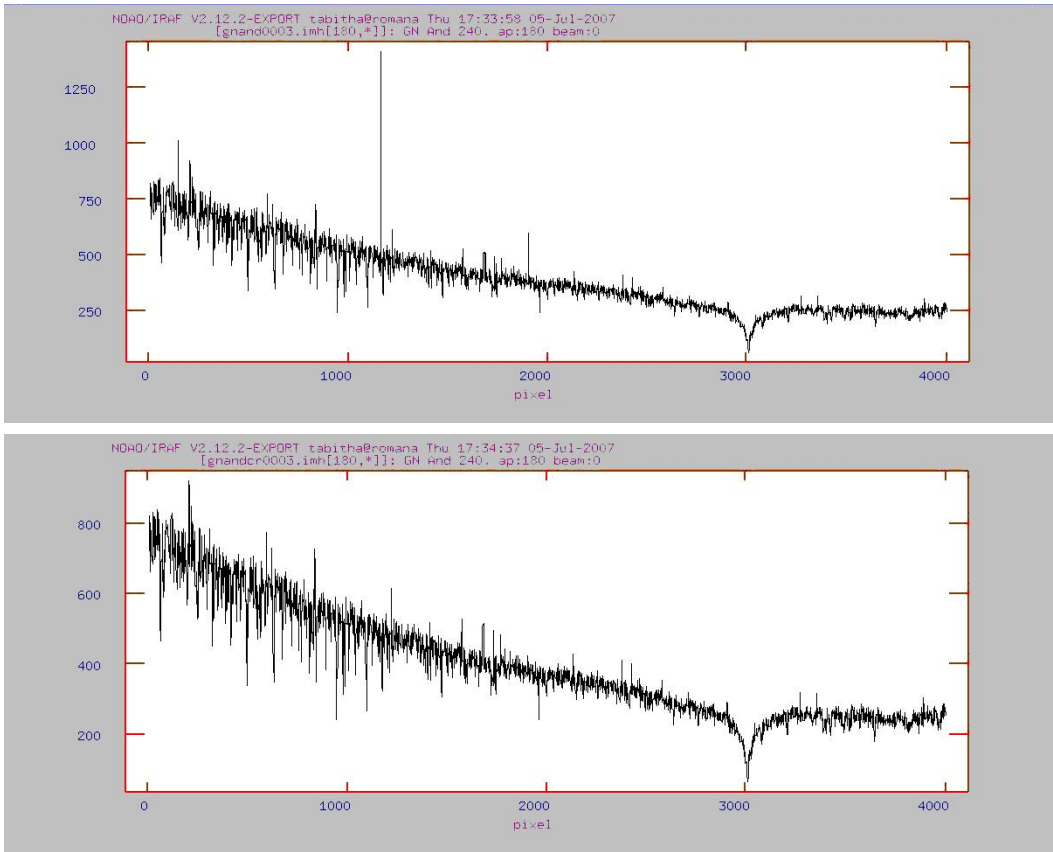
Figure 2.7: A spectrum of GN Andromedae before running through *cosmicrays* (*top*). A spectrum of GN Andromedae after running through *cosmicrays* (*bottom*).

calibration is necessary to ensure that the pixel positions line up with the correct wavelengths. This calibration is called wavelength calibration or dispersion correction, because the dispersion is generally not linear with wavelength in a spectrograph. Arc frames are used for this. An arc frame is a picture of an emission spectrum of a gas, usually iron/argon (FeAr). An arc frame is taken across the same wavelengths as the image spectra. The emission lines in the arcs have a known wavelength. The dispersion is measured by the CCD and the distances on the CCD between the lines are measured. The relationship between CCD position and wavelength is then fit with a low-order polynomial, and this relationship is applied to the image spectra. This matches up the correct wavelengths to the spectral features. The IRAF task *doslit* converts the spectra from two dimensions into one dimension and handles wavelength calibration. Bias- and flat field-corrected spectra and arcs are loaded into *doslit*. Arcs that were obtained on either side of each object, in time, are assigned to be applied to that object, so that two arcs are applied to each object frame. The user defines the aperture for the same reasons and in the same manner as in the flat field frames. The defined aperture is used by *doslit* to subtract out background noise. Spectrum positions on the arc frames are then marked in order for *doslit* to fit a solution to the arcs. In this study, each arc frame was visually compared to a map of an FeAr arc lamp spectrum with a range from 4500 to 5000 Å as shown in Figure 2.8. Four to six spectral lines were identified, marked, and labelled on each arc frame. From that, *doslit* was usually able to find the rest of the dispersion solution and fit a polynomial to it, usually of fourth order. After the dispersion solution was found, it was used to calibrate the object frames so that they were formatted in terms of wavelength instead of pixels. Figure 2.9 shows an object frame before and after wavelength calibration.

2.2.6 Continuum Calibration

For image analysis purposes, object frames are calibrated with the continuum so they can be normalized. This is done in IRAF using the task *continuum*. The
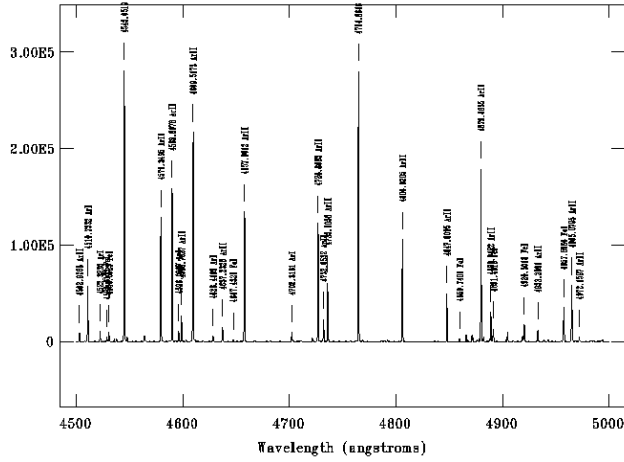
Figure 2.8: FeAr arc map

continuum is determined through fitting a one-dimensional function to it. A predetermined sample of X-values is selected on the spectrum frame and the average of these values is computed. Low- and high-reject values are preset, and if they are greater than zero, the error of the residuals between the fitted points and function is computed. These points are rejected if their residuals meet either of the criteria of Equations 2.1 and 2.2.

$$residual < -rejectvalue_{low} * error \qquad (2.1)$$

$$residual > rejectvalue_{high} * error \qquad (2.2)$$

The function is then refit without the rejected points, and this determines the continuum of the spectrum. Figure 2.10 shows a spectrum of IQ Virginis before and after continuum calibration.
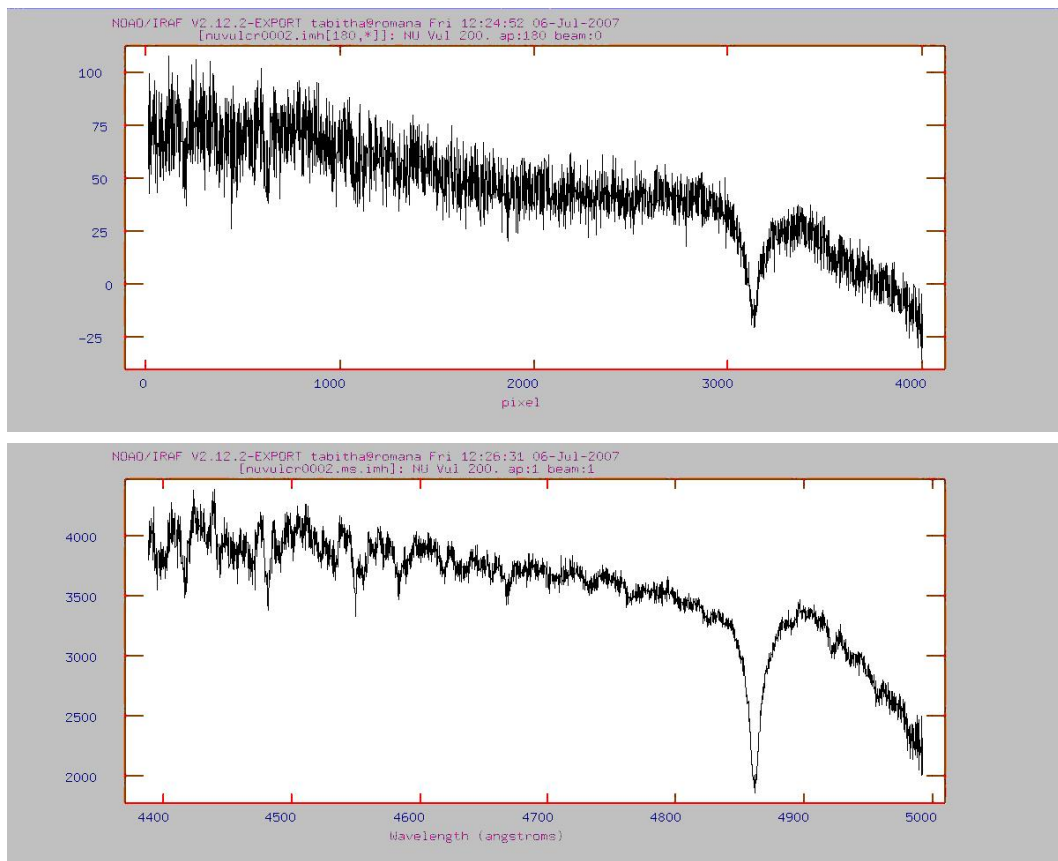
Figure 2.9: A spectrum of NU Vulpeculae before wavelength calibration (*top*). A spectrum of NU Vulpeculae after wavelength calibration (*bottom*).
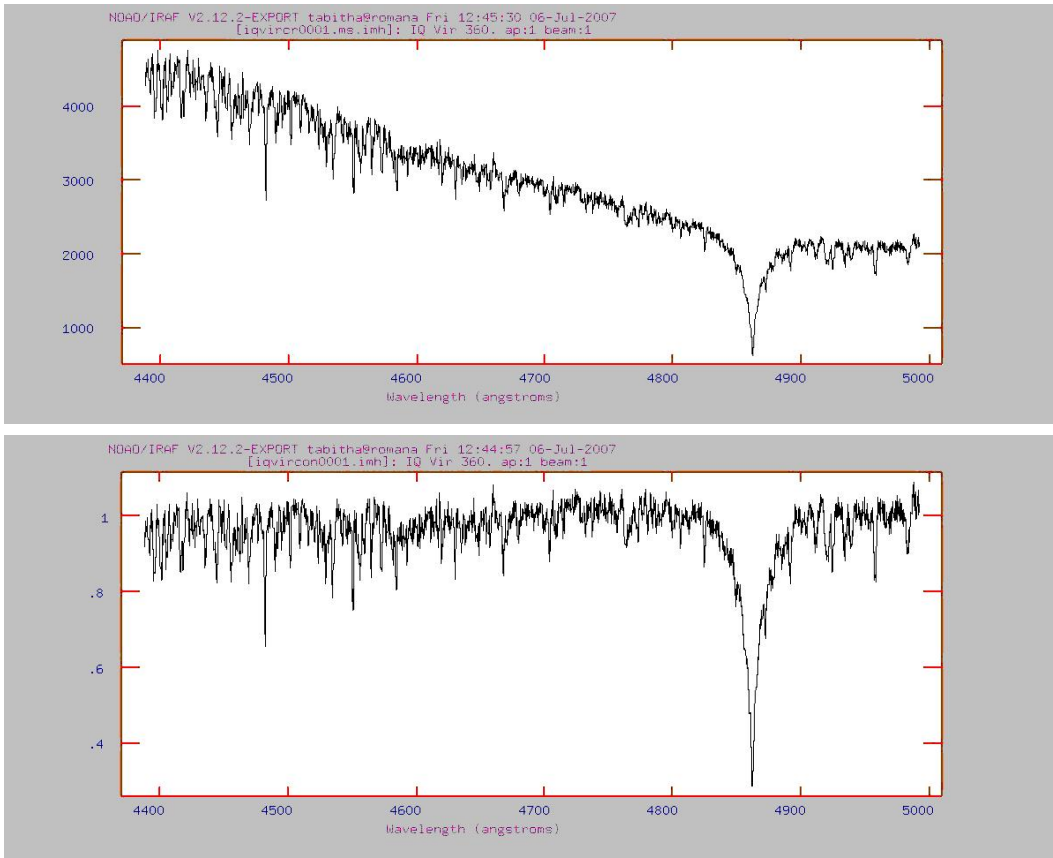
Figure 2.10: A spectrum of IQ Virginis before continuum calibration (*top*). A spectrum of IQ Virginis after continuum calibration (*bottom*).

2.3 Projected Rotational Velocity Methods

A method for calculating projected rotational velocity values was developed and implemented, based on the available data and the work of past authors. The method, adapted from Fekel (1997, 2003), involved finding a relation between previously published $v \sin i$ values and measured spectral feature broadening. The main challenge faced was deciding which spectral feature or features to measure. The MgII line at 4481 Å is a strong line in the spectral range in this study and is therefore easy to measure. Shajn & Struve (1929) measured the MgII line when studying the rotational velocities of B and A stars. Slettebak (1954, 1955) used the MgII line to study rotational velocities over a range of spectral types, including A and F stars, but Slettebak (1955) pointed out that the MgII line is blended with the FeI line at 4482 Å in stars of spectral type F0 and later. Slettebak et al. (1975) used the MgII line to study rotational velocities of stars with spectral types A-F0. Fekel (2003) again pointed out the doublet nature of the MgII line, saying that it may be useful for quickly rotating stars but not for slow rotators. In an effort to attain more consistent results across a range of spectral types and rotational velocities, Fekel (2003) made measurements of five weak to moderate-strength metal lines: TiII at 4501 Å and the FeII lines at 4492 Å , 4508 Å , 4515 Å , and 4523 Å .

Since the MgII line is such a widely measured line, it was also measured in this study. Because the stars in this data set are A and F stars, however, the blending effects in the MgII line were a concern. For this reason, four of the five metal lines used by Fekel (2003) were also measured.

2.3.1 Finding Initial Spectral Broadening

The IRAF task *splot* was used to find line broadening values for each continuum-calibrated spectrum for the stars in the data set. The *splot* task plots spectra and allows for different types of spectral analysis. Each spectrum was plotted in *splot* and zoomed in to the spectral features being measured. FWHM values were calculated for
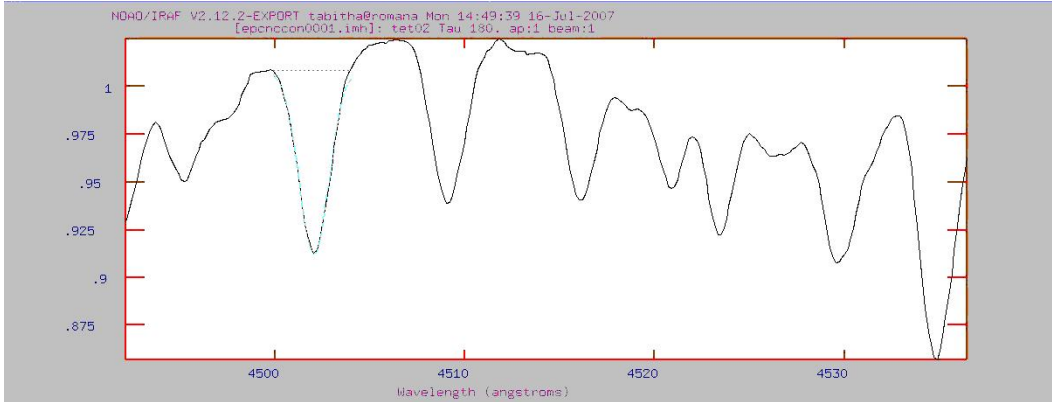
Figure 2.11: Gaussian profile fitting of a spectral line of the star EP Cancri

the 4481 Å MgII line, the 4501 Å TiII line, and the FeII lines at 4508 Å, 4515 Å, and 4523 Å in each spectrum that clearly contained these lines. This was done in *splot* by using the cursor and the *k* key to mark two continuum points, one on each side of the spectral feature. A Gaussian line profile was fit to the spectral feature by *splot*, and the FWHM value of the profile was calculated along with other values such as the center and the equivalent width. Figure 2.11 shows a zoomed-in spectrum with a Gaussian profile fit to the 4501 Å TiII feature. Figure 2.12, adapted from Fekel (2003), shows the spectral features that were measured in this study. Table 2.6 shows which spectral features were measured for each star. Two separate raw broadening values were calculated for each star. The first was the average FWHM value from the MgII line. For the second value, the average FWHM for each of the TiII/FeII spectral features that were measured were averaged together.

Spectral features can be broadened due to just the instrumentation. For each night of observing, an arc lamp frame was analyzed to remove instrumental broadening. The amount of broadening in the arc lamp features can be subtracted from the spectral line broadening for each observation so that instrumental broadening is not mistaken for rotational broadening. The FWHM values of several arc lines were measured in *splot* and averaged together for one arc frame from each observation

Table 2.6.   Spectral Features Measured

Star	Spectral Features Measured (Å)	Star	Spectral Features Measured (Å)
41 Peg	4481, 4508	V340 And	4481, 4508
AI CVn	4501, 4508, 4515	V352 Aur	4481, 4501, 4508, 4515, 4523
AO CVn	4481, 4501, 4508, 4515, 4523	V376 Per	4481, 4501, 4508, 4515
AZ CMi	4481, 4501, 4508, 4515, 4523	V377 Cep	4481, 4501, 4508
BT Cnc	4481, 4501, 4508	V386 Per	4481, 4501, 4508
CL Dra	4481, 4501, 4508, 4515	V388 Cep	4481, 4508
CN Boo	4481, 4501, 4508, 4515, 4523	V480 Tau	4481, 4501, 4508
CN Dra	4481, 4501, 4508, 4515, 4523	V483 Tau	4481, 4501, 4508, 4515
CO Lyn	4501, 4508, 4515, 4523	V509 Per	4481, 4501, 4508, 4515
CX Cnc	4481, 4501, 4508	V521 Per	4481, 4523
CX UMa	4523	V526 Cas	4481, 4501, 4508, 4515, 4523
DD UMa	4481, 4501, 4508	V620 Her	4481, 4501, 4508
DK Vir	4481, 4501, 4508, 4515	V644 Her	4481, 4501, 4508, 4515, 4523
DP UMa	4481, 4501, 4508, 4515, 4523	V696 Tau	4481, 4501, 4508, 4523
EM Aqr	4481, 4501, 4508, 4515	V775 Tau	4481, 4501, 4508, 4515, 4523
EN UMa	4501, 4508, 4515	V777 Tau	4481, 4501, 4508
EP Cnc	4481, 4501, 4508, 4515, 4523	V784 Cas	4481, 4501, 4508, 4523
ER Dra	4481, 4501, 4508, 4515, 4523	V831 Her	4481, 4508, 4515, 4523
FI UMa	4481, 4501, 4508	V1004 Ori	4481, 4501, 4508, 4515, 4523
FM Com	4481, 4501, 4508	V1208 Aql	4481, 4501, 4508, 4515, 4523
FM Vir	4481, 4501, 4508, 4515, 4523	V1276 Cyg	4481, 4501, 4508, 4515, 4523
FP Ser	4501	V1431 Aql	4481, 4508
FQ Boo	4523	V1644 Cyg	4481, 4501, 4508
GG Vir	4481, 4501, 4508	V2112 Oph	4481, 4501, 4508
GN And	4481, 4501, 4508, 4515, 4523	VV Ari	4481, 4501, 4508, 4515, 4523
GX Peg	4481, 4501, 4508, 4508	VW Ari	4481, 4501, 4508, 4515
HT Peg	4481, 4501, 4508	VX Psc	4481, 4508
II Vir	4523	VY Psc	4481, 4501, 4508, 4515, 4523
IK Peg	4481, 4501	XX Psc	4481, 4508
IM Tau	4481, 4501, 4508, 4515, 4523	β Cas	4481, 4501, 4508, 4515
IQ Vir	4481, 4501, 4508, 4515, 4523	β Vir	4508, 4515, 4523
KW 284	4481, 4501, 4508, 4515	γ Boo	4481, 4501, 4508
KW Aur	4501, 4508, 4515, 4523	δ Del	4481, 4501, 4508, 4515, 4523
LT Vul	4481, 4501, 4508	δ Ser	4481, 4501, 4508, 4515, 4523
NU Vul	4481, 4501, 4508	ϵ Cep	4501, 4508, 4515, 4523
OX Aur	4481, 4501, 4508	θ2 Tau	4481, 4501, 4508, 4515
RX Sex	4523	ι Boo	4481, 4501, 4508, 4515
SAO 52892	4481, 4508	κ2 Boo	4501, 4508, 4515
SAO 72399	4481, 4508	λ Boo	4481, 4501, 4508, 4515, 4523
SAO 88295	4508, 4515	ν UMa	4481, 4501, 4508
SAO 141427	4481, 4501, 4508, 4515	ρ Tau	4481, 4501, 4508, 4515
SAO 143373	4481, 4501, 4508	τ Peg	4481, 4501, 4508, 4515
UU Ari	4481, 4501, 4508	υ Tau	4481, 4501, 4508
UV Ari	4481, 4501, 4508, 4515, 4523		
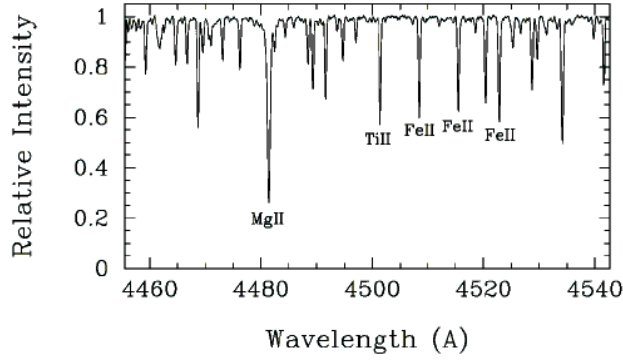
Figure 2.12: Spectral features measured for $v\sin(i)$ analysis. Image from Fekel (2003).
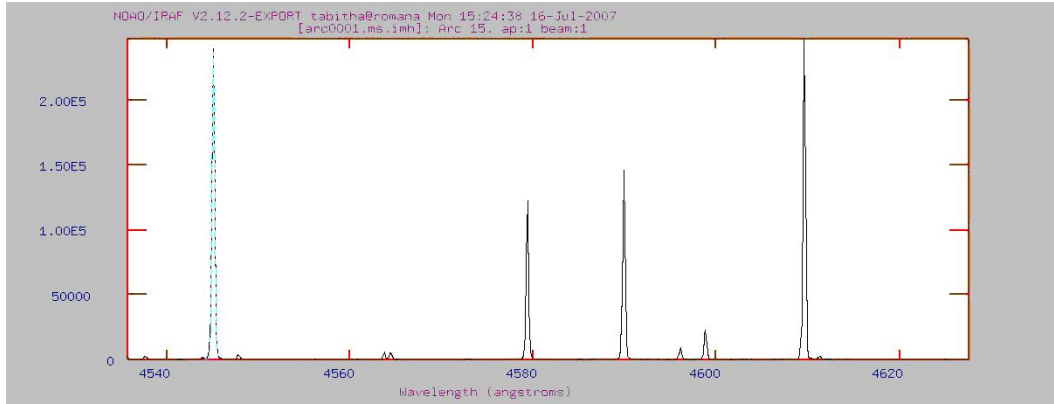
Figure 2.13: Gaussian profile fitting of an arc lamp line.

night. The average instrumental broadening for the data set was 0.318 Å. Figure 2.13 shows a zoomed-in view of an arc being measured. The instrumental broadening was removed from each raw broadening value in the same manner as in Fekel (1997, 2003), by taking the square root of the difference of the two squares, as given in Equation 2.3.

$$broad_{ROT} = \sqrt{(FWHM_{spect})^2 - (FWHM_{arc})^2} \tag{2.3}$$

Removing the instrumental broadening resulted in the initial rotational broadening values, assumed to be due to rotation, both for the MgII measurements and the TiII/FeII measurements.

40

2.4 Finding Initial Hydrogen-Beta Values

The IRAF task *sbands* was used to calculate Hβ color index values for each observation. Each observation night was run through *sbands* separately. For each night, *sbands* requires three text files: a list of input spectra, a bandpass file, and a filter function file. The first file simply lists each individual spectrum that was acquired that night and selected to be run through *sbands*. The bandpass file has four fields: an identification name, the central wavelength of the bandpass, the width of the bandpass, and the name of the corresponding filter function file. If no filter function file is specified, a square filter is assumed. Two bandpasses, such as Hβ-narrow and Hβ-wide, can go in the same bandpass file. The filter function file is a wavelength-ordered list of wavelength and filter response at that wavelength, in percentage. Both square and Gaussian filter functions were used for the Hβ filters. For the Gaussian filters, the response relation used is given in Equation 2.4.

$$y = a \exp\left[-(x - b)^2/c^2\right] \tag{2.4}$$

In Equation 2.4, y is the relative response, a is the peak height of the Gaussian curve, x is wavelength value, b is the central wavelength of the filter function, and c is given by Equation 2.5.

$$c = FWHM/2\sqrt{\ln(2)} \tag{2.5}$$

For all of the filter functions, 4861 Å was given as the central wavelength. The relative peak height of the Gaussian Hβ-wide filter function was entered as 0.70 and the FWHM value was 150 Å. The Gaussian Hβ-narrow peak was given as 0.62 and the FWHM value was 30 Å (see Figure 1.12). A list of wavelength values was made, in increments of 0.01 Å, and entered into Equation 2.4. This resulted in the list of filter responses needed for the filter function file. The Gaussian filters were cut off at the FWHM values, as shown in Figure 2.14. This resulted in squared-off
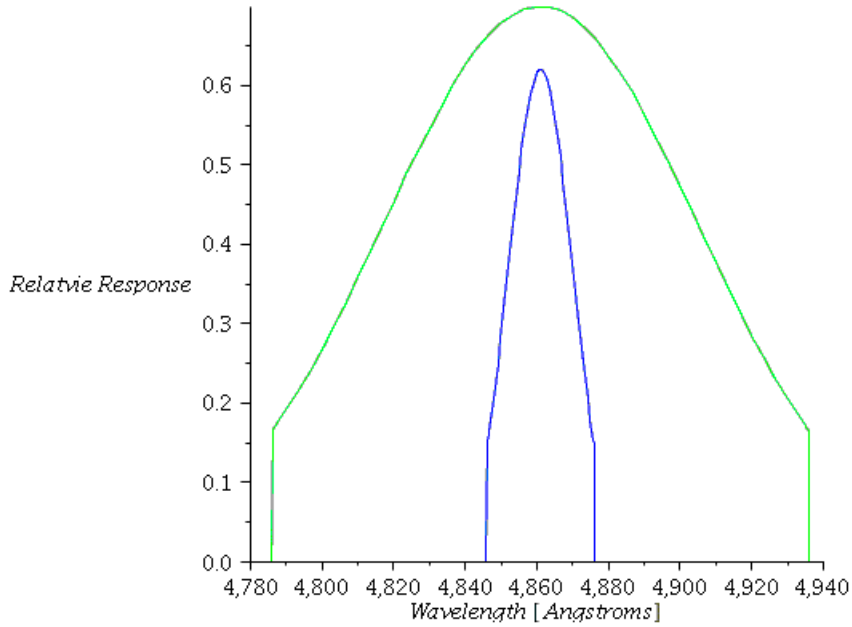
Figure 2.14: Profiles of theoretical Gaussian wide and narrow Hβ filters.

Gaussian filter functions. Equation 2.6 was used by *sbands* to calculate the flux from a spectrum in each bandpass.

$$flux = \sum pix_n response_n \tag{2.6}$$

In Equation 2.6, pix_n is each pixel in the interval, and $response_n$ is the filter response at that pixel. Each Hβ flux value was then converted to a magnitude value by *sbands* using Equation 2.7.

$$mag = magzero - 2.5 \log{(flux)} \tag{2.7}$$

In Equation 2.7, *magzero* is a parameter for the zeropoint magnitude. If two bandpasses are being run through *sbands*, as in this case, *sbands* reports the magnitudes of the different bandpasses as well as the difference in magnitudes. This yields the Hβ color index. Figure 2.15 shows an *sbands* output file. Two nights

```
SBANDS: NOAO/IRAF V2.12.2-EXPORT tabitha@romana Wed 13:34:40 01-Aug-2007
   bands = newbandpass, norm = no, mag = yes, magzero = 0.00
      band     filter wavelength       width
betanarrow betanarrowfunction.txt      4860.        30.
  betawide betawidefunction.txt        4860.       150.

                  spectrum    band        mag  band        mag     index   eqwidth
         41pegbeta0001.imh(1) betanar  -4.48395 betawid  -6.78402  2.30006  26.3934
         41pegbeta0002.imh(1) betanar  -4.4455  betawid  -6.78365  2.33815  26.5177
         41pegbeta0003.imh(1) betanar  -4.48755 betawid  -6.78069  2.29314  26.3703
      sao52892beta0001.imh(1) betanar  -4.50608 betawid  -6.78388  2.2778   26.3187
      sao52892beta0002.imh(1) betanar  -4.45438 betawid  -6.74813  2.29375  26.3724
      sao52892beta0003.imh(1) betanar  -4.52947 betawid  -6.77973  2.25026  26.2241
      sao72399beta0001.imh(1) betanar  -4.37037 betawid  -6.74229  2.37192  26.6244
      sao72399beta0002.imh(1) betanar  -4.42995 betawid  -6.75583  2.32587  26.4781
      sao72399beta0003.imh(1) betanar  -4.4791  betawid  -6.78904  2.30993  26.4261
       v340andbeta0001.imh(1) betanar  -4.46406 betawid  -6.77288  2.30883  26.4224
       v340andbeta0002.imh(1) betanar  -4.49399 betawid  -6.77829  2.2843   26.3407
       v340andbeta0003.imh(1) betanar  -4.46001 betawid  -6.77639  2.31638  26.4472
       v377cepbeta0001.imh(1) betanar  -4.61968 betawid  -6.81477  2.19509  26.0273
       v377cepbeta0002.imh(1) betanar  -4.70333 betawid  -6.83961  2.13628  25.8062
       v377cepbeta0003.imh(1) betanar  -4.7673  betawid  -6.95127  2.18396  25.9864
       v388cepbeta0001.imh(1) betanar  -4.60262 betawid  -6.79796  2.19534  26.0282
       v388cepbeta0002.imh(1) betanar  -4.62868 betawid  -6.79925  2.17058  25.9366
       v388cepbeta0003.imh(1) betanar  -4.70615 betawid  -6.8423   2.13615  25.8057
        vxpscbeta0001.imh(1) betanar  -4.59794 betawid  -6.81921  2.22127  26.1219
        vxpscbeta0002.imh(1) betanar  -4.52074 betawid  -6.7871   2.26636  26.2797
        vxpscbeta0003.imh(1) betanar  -4.5463  betawid  -6.78563  2.23934  26.186
        vxpscbeta0004.imh(1) betanar  -4.50859 betawid  -6.77841  2.26982  26.2915
        vxpscbeta0005.imh(1) betanar  -4.51324 betawid  -6.77908  2.26584  26.2779
        vxpscbeta0006.imh(1) betanar  -4.59427 betawid  -6.79993  2.20566  26.0658
        xxpscbeta0001.imh(1) betanar  -4.56131 betawid  -6.79632  2.23501  26.1707
        xxpscbeta0002.imh(1) betanar  -4.61104 betawid  -6.79864  2.1876   25.9998
        xxpscbeta0003.imh(1) betanar  -4.5494  betawid  -6.78706  2.23766  26.18
```

Figure 2.15: *sbands* output file

in the data set, 13 August 2002 and 15 August 2002, had seven stars each with at least three observations. Raw Hβ color index values were found for the Gaussian and square filter functions, on both continuum-calibrated and non continuum-calibrated spectra using *sbands*, resulting in four combinations. Table 2.7 gives the average values found, along with the values found in the Rodriguez et al. (2000) catalog. To show the spread in the calculations, Table 2.8 gives the standard deviations in the values found. The average standard deviation for the Gaussian continuum-calibrated combination was 0.023 mag, for the Gaussian non continuum-calibrated combination it was 0.025 mag, for the square continuum-calibrated combination it was 0.023 mag, and for the square non continuum-calibrated combination it was 0.027 mag.

Table 2.7.   Average Raw Hβ Color Index Values

Star	Gaussian Filters		Square Filters		Rodriguez et al. (2000) Hβ
	Cont Hβ	Non-cont Hβ	Cont Hβ	Non-cont Hβ	
41 Peg	2.310	2.320	2.154	2.164	2.872
LT Vul	2.179	2.178	2.019	2.019	2.749
SAO 52892	2.274	2.284	2.124	2.137	2.834
SAO 72399	2.336	2.342	2.184	2.193	2.888
V340 And	2.303	2.311	2.151	2.162	2.878
V388 Cep	2.167	2.167	2.017	2.017	2.734
V526 Cas	2.211	2.239	2.055	2.069	2.770
V1208 Aql	2.221	2.228	2.066	2.078	2.796
V1276 Cyg	2.168	2.176	2.014	2.027	2.732
V1644 Cyg	2.246	2.249	2.091	2.100	2.832
V2112 Oph	2.159	2.151	1.995	2.001	2.724
VX Psc	2.245	2.243	2.088	2.091	2.817
VY Psc	2.216	2.188	2.047	2.039	2.777
XX Psc	2.220	2.227	2.071	2.080	2.773

Table 2.8.   Standard Deviations of Calculated Raw Hβ Color Index Values

Star	Gaussian Filters		Square Filters	
	Cont Hβ	Non-cont Hβ	Cont Hβ	Non-cont Hβ
41 Peg	0.024	0.031	0.022	0.030
LT Vul	0.015	0.016	0.016	0.020
SAO 52892	0.022	0.027	0.021	0.027
SAO 72399	0.032	0.039	0.031	0.040
V340 And	0.017	0.017	0.016	0.017
V388 Cep	0.029	0.036	0.032	0.041
V526 Cas	0.017	0.007	0.016	0.019
V1208 Aql	0.017	0.019	0.016	0.018
V1276 Cyg	0.021	0.023	0.020	0.023
V1644 Cyg	0.009	0.010	0.010	0.010
V2112 Oph	0.025	0.027	0.024	0.027
VX Psc	0.023	0.026	0.026	0.028
VY Psc	0.047	0.043	0.044	0.041
XX Psc	0.028	0.033	0.025	0.032

Chapter 3

# Analysis and Results

3.1   Analysis of Broadening Values

Using a method similar to those used by Fekel (1997, 2003), the spectral broadening values were plotted against previously published $v \sin i$ values. The $v \sin i$ values found in the Rodriguez et al. (2000) catalog were used for stars in common. The $v \sin i$ values for the two rotational velocity standards were found in Slettebak et al. (1975). This plot was made for both the MgII measurements and the TiII/FeII measurements. A second-order polynomial was fitted to each plot as a calibration curve. For the MgII relation, however, a linear fit was better. Figure 3.1 shows the two initial plots with the calibration curves. The calibration curves are given by Equations 3.1 and 3.2. In the equations that follow, y represents $v \sin i$, and x represents the spectral broadening values.

$$y_{TiII/FeII} = -(7.7 \pm 3.9)x^2 + (98.8 \pm 21.6)x - (69.7 \pm 29.9), R = 0.82 \qquad (3.1)$$

$$y_{MgII} = (61.8 \pm 5.6)x - (79.2 \pm 17.3), R = 0.80 \qquad (3.2)$$

In order to see how the calibration would vary with each of the four TiII/FeII spectral features, a calibration plot was made for each of the spectral features measured. Figure 3.2 shows these four plots. Equations 3.3 through 3.6 describe the calibration curves for the plots, in the same order the plots are given.

$$y_{4501} = -(17.7 \pm 4.8)x^2 + (151.4 \pm 26.5)x - (136.2 \pm 33.2), R = 0.82 \qquad (3.3)$$
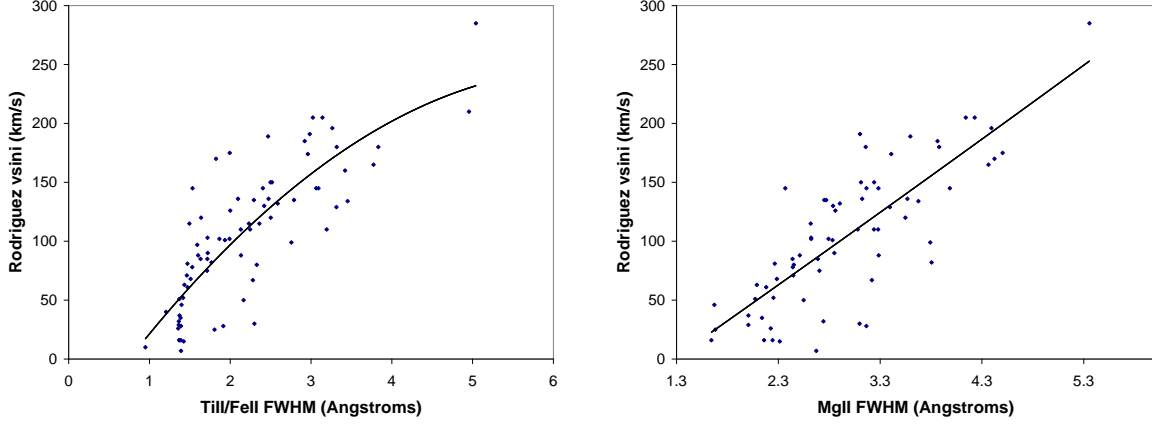
Figure 3.1: Initial spectral broadening relation for TiII/FeII measurements (*left*), and MgII measurements (*right*).

$$y_{4508} = -(7.8 \pm 6.8)x^2 + (96.7 \pm 32.4)x - (75.4 \pm 36.6), R = 0.78 \qquad (3.4)$$

$$y_{4515} = -(16.9 \pm 7.4)x^2 + (133.1 \pm 36.4)x - (99.5 \pm 42.9), R = 0.67 \qquad (3.5)$$

$$y_{4523} = (21.3 \pm 10.0)x^2 - (75.2 \pm 58.9)x + (117.3 \pm 58.4), R = 0.76 \qquad (3.6)$$

The fits for the 4501 Å TiII relation and the 4508 Å FeII relation were stronger than the other two and had the higher degrees of correlation. These two spectral features were also measured in a greater percentage of the stars in the data set. Therefore, to tighten up the calibration curve, a new relation was found for the TiII/FeII measurements, using only the TiII 4501 Å line and the FeII 4508 Å line FWHM values averaged together. Stars were only included in the relation if they had

46
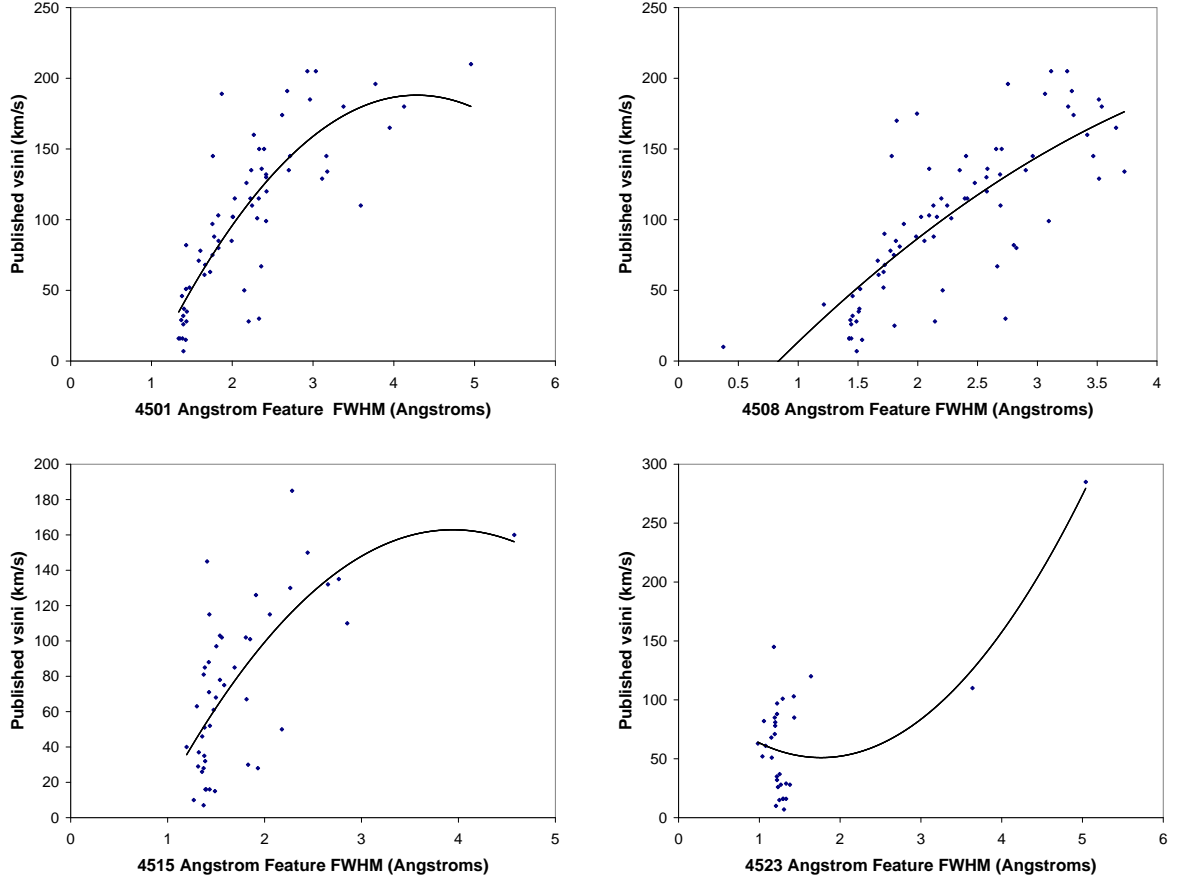
Figure 3.2: Calibration plot for TiII 4501 Å feature (*top-left*), FeII 4508 Å feature (*top-right*), FeII 4515 Å feature (*bottom-left*), and FeII 4523 Å feature (*bottom-right*).

at least three measurements of each spectral feature. The stars and the values plotted for them are listed in Table 3.1. The relation is plotted in Figure 3.3 and given by Equation 3.7.

$$y_{newTi/Fe} = -(26.3 \pm 9.7)x^2 + (196.7 \pm 47.0)x - (198.7 \pm 53.9), R = 0.84 \qquad (3.7)$$

To check the internal consistency of the TiII 4501 Å and FeII 4508 Å measurements, a linear regression was run relating the FWHM values of each feature for

47

Table 3.1.   Stars Used for TiII/FeII Relation with at Least Three Measurements
Each

| Star	FWHM (Å)	Rodriguez $v \sin i$ (km/s)	Star	FWHM (Å)	Rodriguez $v \sin i$ (km/s)
AI CVn	2.114	115	UV Ari	2.933	68
AO CVn	1.512	15	V376 Per	4.097	102
AZ CMi	1.492	35	V386 Per	8.412	129
CL Dra	2.603	150	V483 Tau	4.532	102
CN Dra	2.041	85	V526 Cas	2.000	16
CX Cnc	2.547	120	V620 Her	9.663	191
DD UMa	3.002	145	V644 Her	2.051	16
DP UMa	1.744	78	V775 Tau	2.081	32
EM Aqr	2.634	132	V777 Tau	7.197	196
EP Cnc	1.778	145	V1004 Ori	2.719	71
FI UMa	3.342	145	V1208 Aql	2.250	51
FM Com	3.656	180	V1276 Cyg	4.136	103
FM Vir	2.155	28	V1644 Cyg	6.992	80
GN And	1.408	16	V2112 Oph	6.968	189
GX Peg	1.444	46	VY Psc	4.078	101
HT Peg	3.687	165	β Cas	3.324	50
IK Peg	1.490	37	γ Boo	5.667	115
IM Tau	1.471	7	δ Del	2.025	29
IQ Vir	1.669	61	ϵ Cep	3.451	97
KW 284	2.653	30	θ^2 Tau	4.888	67
KW Aur	1.476	28	ι Boo	6.469	130
LT Vul	2.539	136	κ^2 Boo	5.644	115
NU Vul	3.143	205	λ Boo	7.382	110
OX Aur	3.618	134	ν UMa	5.044	110
SAO 141427	3.422	185	ρ Tau	5.839	126
SAO 143373	2.327	135	τ Peg	8.192	135
UU Ari	3.165	174	υ Tau	7.181	205
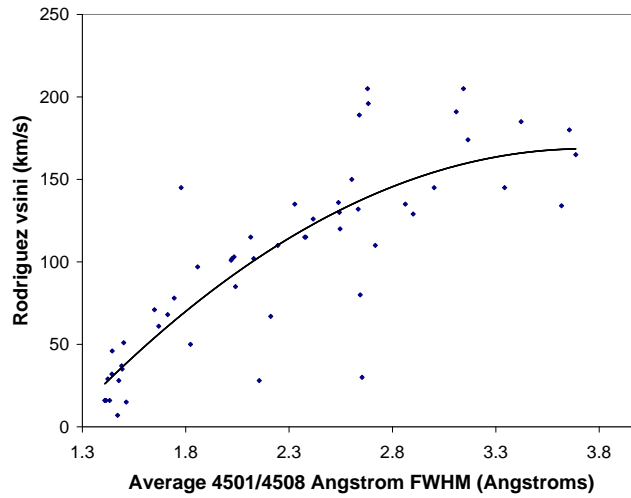
Figure 3.3: Broadening calibration using TiII 4501 Å and FeII 4508 Å features
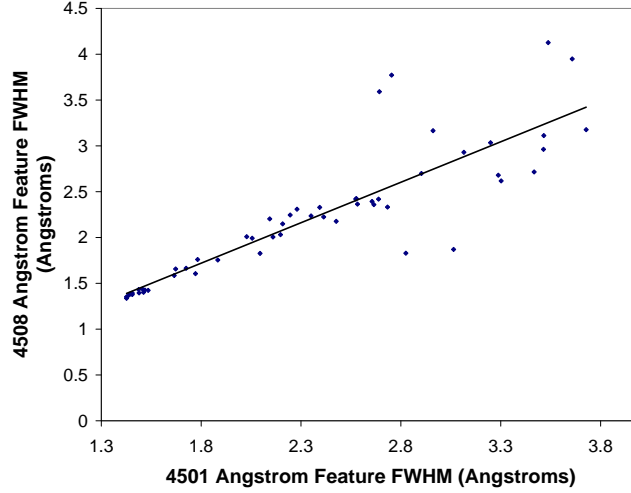
Figure 3.4: Consistency check between TiII 4501 Å and FeII 4508 Å FWHM values

every star that had at least three measurements for each feature. This regression is shown in Figure 3.4 and given by Equation 3.8. The relation appears to be linear up to a TiII 4501 Å feature FWHM value of about 2.7 Å. From this, it would be expected that any $v \sin i$ relation found with these measurements would also break down at a TiII 4501 Å FWHM value of about 2.7 Å.

$$y_{internal} = (0.9 \pm 0.1)x + (0.1 \pm 0.2), R = 0.87 \qquad (3.8)$$

Next, a new MgII/$v \sin i$ relation was plotted, using the average FWHM values of only the stars that had at least three MgII measurements. The stars and their plotted values are shown in Table 3.2. This plot is given in Figure 3.5, with the relation given by Equation 3.9.

$$y_{newMg} = (62.0 \pm 6.5)x - (78.7 \pm 19.6), R = 0.79 \qquad (3.9)$$

Next, standard deviations were calculated for the values that went into the FWHM averages for each spectral feature. To refine each relation, data for stars

Table 3.2. Stars Used for MgII Relation with at Least Three Measurements

| Star	FWHM (Å)	Rodriguez $v \sin i$ (km/s)	Star	FWHM (Å)	Rodriguez $v \sin i$ (km/s)
41 Peg	1.680	25	UV Ari	2.285	68
AO CVn	2.314	15	V340 And	3.286	88
AZ CMi	2.140	35	V376 Per	2.623	102
CL Dra	3.112	150	V386 Tau	3.395	129
CN Dra	2.439	85	V526 Cas	2.243	16
CX Cnc	3.548	120	V620 Her	3.102	191
DD Uma	3.283	145	V644 Her	2.160	16
DP Uma	2.442	78	V775 Tau	2.743	32
EM Aqr	2.904	132	V777 Tau	4.393	196
EP Cnc	2.368	145	V831 Tau	2.265	81
ER Dra	2.089	63	V1004 Ori	2.447	71
FI Uma	3.165	145	V1208 Aql	2.073	51
FM Com	3.880	180	V1276 Cyg	2.622	103
FM Vir	3.165	28	V1644 Cyg	2.451	80
GN And	1.642	16	V2112 Oph	3.596	189
GX Peg	1.672	46	VX Psc	3.568	136
HT Peg	4.365	165	VY Psc	2.832	101
IK Peg	2.006	37	XX Psc	4.424	170
IM Tau	2.672	7	β Cas	2.548	50
IQ Vir	2.181	61	γ Boo	2.618	115
KW 284	3.097	30	δ Del	2.006	29
LT Vul	3.124	136	θ^2 Tau	3.219	67
NU Vul	4.141	205	ι Boo	2.837	130
OX Aur	3.676	134	λ Boo	3.240	110
SAO 52892	4.503	175	ν UMa	3.081	110
SAO 72399	3.281	110	ρ Tau	2.860	126
SAO 141427	3.863	185	τ Peg	2.751	135
SAO 143373	2.770	135	υ Tau	4.229	205
UU Ari	3.409	174			
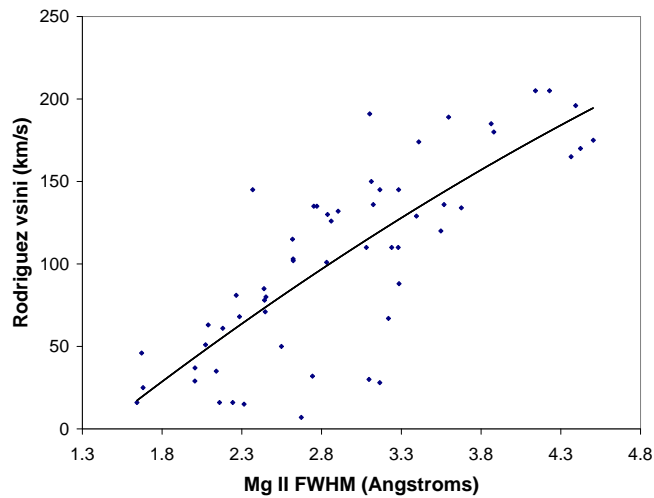
Figure 3.5: Plot of MgII feature FWHM vs. $v \sin i$ for at least three observations of each star

Table 3.3. Stars Rejected Due to High Standard Deviations

Star	V mag	Spectral Feature (Å)	Standard Deviation in Measurements (Å)
CX Cnc	6.05	4481	0.430
		4508	0.543
DD UMa	4.80	4508	0.521
FI UMa	6.63	4501	0.436
FM Com	6.46	4501	1.702
		4508	0.800
HT Peg	5.30	4501	0.954
		4508	0.623
NU Vul	5.19	4501	0.517
		4508	0.552
OX Aur	6.10	4501	0.410
SAO 141427	6.25	4501	0.466
		4508	0.319
UU Ari	6.14	4501	0.479
V386 Per	6.54	4508	0.596
V620 Her	6.20	4508	0.304
V777 Tau	4.48	4501	1.335
		4508	0.559
V1644 Cyg	4.93	4481	0.576
		4501	0.435
		4508	1.134
V2112 Oph	6.51	4501	0.609
		4508	0.471
VX Psc	6.01	4481	0.489
VY Psc	6.55	4481	0.358
		4501	0.742
		4508	0.545
λ Boo	4.18	4501	1.958
		4508	1.887
ν UMa	3.78	4508	0.375
τ Peg	4.58	4508	0.333

with a standard deviation greater than 0.3 Å were rejected from the relations. Over half of these stars were dimmer than 6th magnitude. The data rejected from each relation, along with the standard deviations, are given in Table 3.3. The new plots and relations are shown in Figure 3.6 and given in Equations 3.10 and 3.11.

$$y_{refinedTi/Fe} = -(46.8 \pm 37.7)x^2 + (273.7 \pm 151.5)x - (268.4 \pm 145.9), R = 0.78 \quad (3.10)$$

$$y_{refinedMg} = (62.7 \pm 6.8)x - (80.5 \pm 20.5), R = 0.79 \quad (3.11)$$
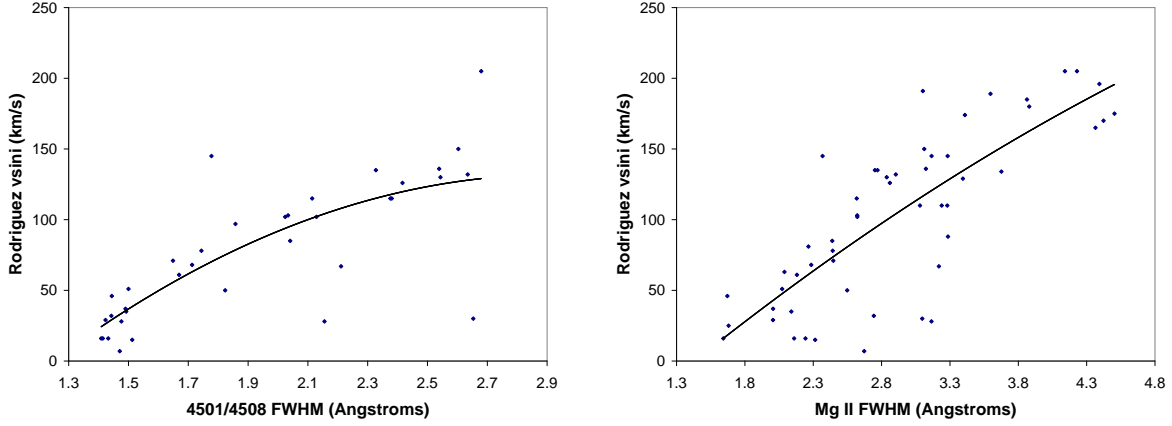
Figure 3.6: $v \sin i$ relations after rejecting high standard deviations for TiII/FeII measurements (*left*), and MgII measurements (*right*).

More recently published $v \sin i$ values were found in Royer et al. (2002b) for the stars remaining in the relation. These values are more internally consistent because the values came from the same source, using the same method, rather than from a variety of sources. A plot for each set of measurements was made with the Royer et al. (2002b) values. Table 3.4 gives both the Rodriguez et al. (2000) and Royer et al. (2002b) $v \sin i$ values for the remaining stars. The plots using the Royer et al. (2002b) $v \sin i$ values are given in Figure 3.7, and the relations are given by Equations 3.12 and 3.13.

$$y_{royerTi/Fe} = (113.7 \pm 10.6)x - (128.9 \pm 20.9), R = 0.90 \tag{3.12}$$

$$y_{royerMg} = (67.0 \pm 7.0)x - (78.0 \pm 21.1), R = 0.83 \tag{3.13}$$

In order to make sure the relations were not biased toward either catalog, both the Rodriguez et al. (2000) and Royer et al. (2002b) $v \sin i$ values for stars found in both catalogs were used in the same plots. These relations are shown in Figure 3.8 and given in Equations 3.14 and 3.15.

Table 3.4. $v \sin i$ Values from Royer et al. (2002b) and Rodriguez et al. (2000) Catalogs

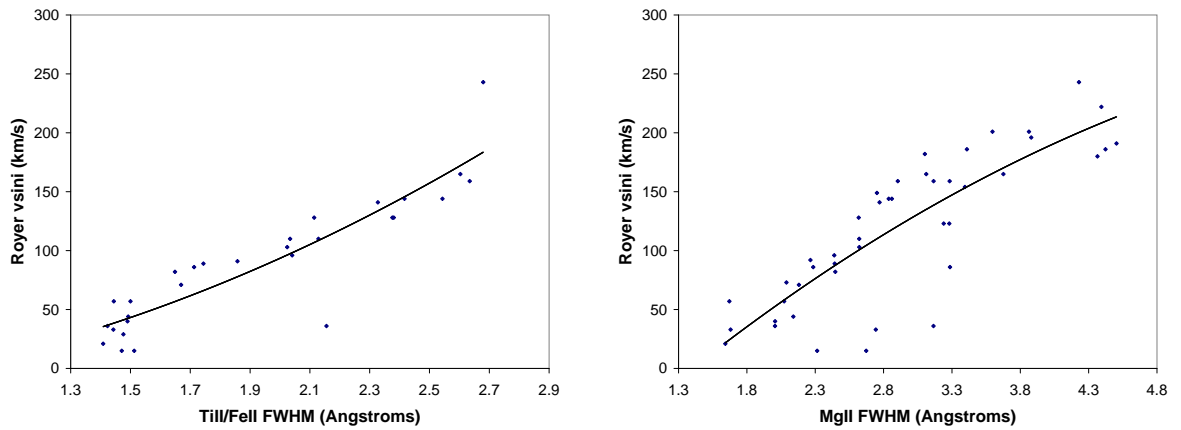| Star	Royer $v \sin i$ (km/s)	Rodriguez $v \sin i$ (km/s)
AI CVn	128	115
AO CVn	15	15
AZ CMi	44	35
CL Dra	165	150
CN Dra	96	85
DP UMa	89	78
EM Aqr	159	132
FM Vir	36	28
GN And	21	16
GX Peg	57	46
IK Peg	40	37
IM Tau	15	7
IQ Vir	71	61
KW Aur	29	28
SAO 143373	141	135
UV Ari	86	68
V376 Per	103	102
V483 Tau	110	102
V775 Tau	33	32
V1004 Ori	82	71
V1208 Aql	57	51
V1276 Cyg	110	103
γ Boo	128	115
δ Del	36	29
ϵ Cep	91	97
ι Boo	144	130
κ^2 Boo	128	115
ρ Tau	144	126
υ Tau	243	205

Figure 3.7: $v \sin i$ relations using Royer et al. (2002b) $v \sin i$ values for TiII/FeII measurements (*left*), and MgII measurements (*right*).
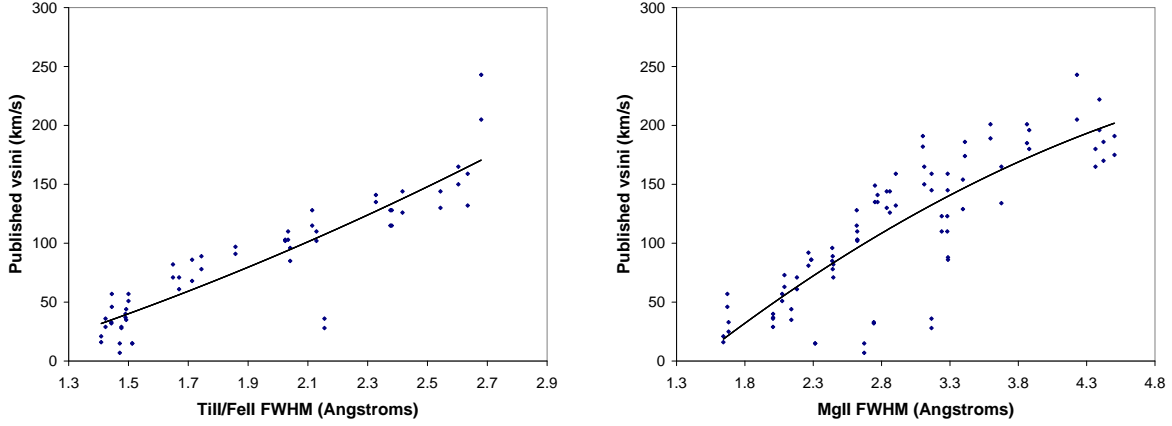
Figure 3.8: $v \sin i$ relations using Rodriguez et al. (2000) & Royer et al. (2002b) $v \sin i$ values for TiII/FeII measurements (*left*), and MgII measurements (*right*).

$$y_{rodroyTi/Fe} = (107.6 \pm 7.2)x - (122.1 \pm 14.2), R = 0.89 \tag{3.14}$$

$$y_{rodroyMg} = -(8.0 \pm 5.6)x^2 + (113.1 \pm 34.8)x - (145.6 \pm 51.6), R = 0.82 \tag{3.15}$$

The tightest of these two relations, the TiII/FeII relation, was refined a little more to make the final relation. It is evident from looking at Figure 3.8 that $v \sin i$ values of 40 km/s or less cannot be distinguished with this relation, so these data points were removed from the relation. A Thompson t-test was run on the remaining relation, using a linear fit, to determine that v Tau was an outlier. v Tau is not a particularly bright star in the data set, and no other anomalous characteristics about it were found to suggest that it is part of another population. This point was rejected from the relation, with the further justification that it lies beyond the end of the relation and is an influential point, weighted more heavily, that could skew the relation. The final relation is shown in Figure 3.9 and given by Equation 3.16.
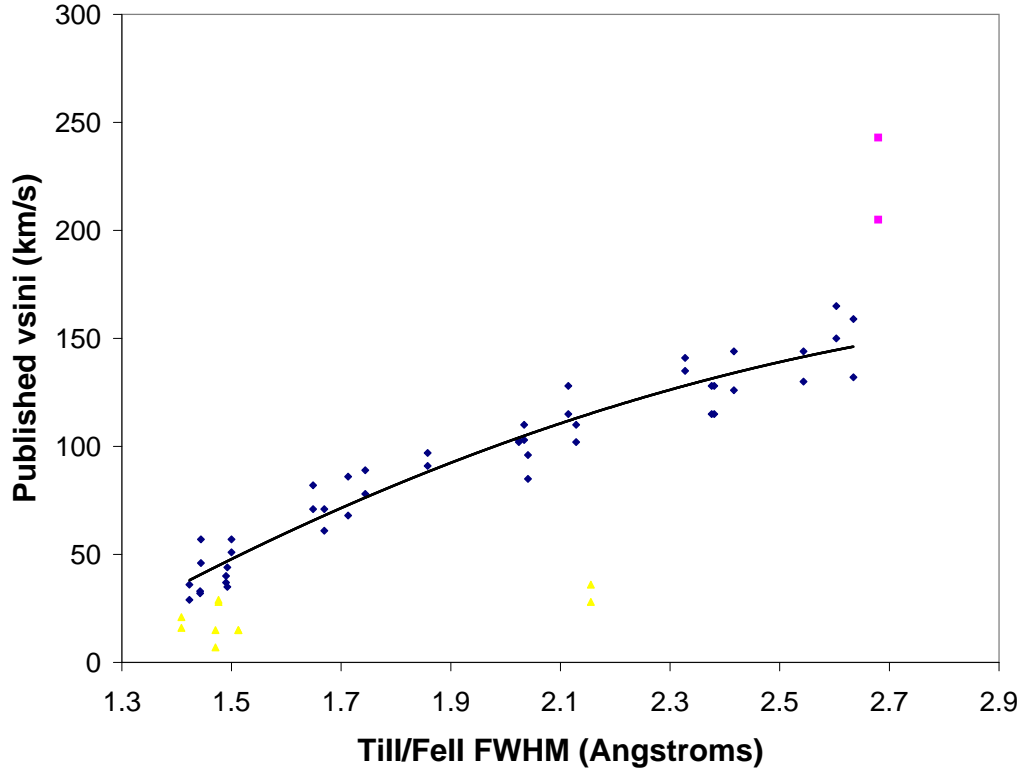
Figure 3.9: Final $v \sin i$ calibration relation. Each star is represented by two separate data points (one from each catalog). The triangle-shaped data points represent stars with $v \sin i$ values below 40 km/s, and the two square data points represent the star v Tau, an outlier.

Using this relation, an average FWHM value can be used as the variable x to find a rotational velocity value, y.

$$y_{final} = -(33.7 \pm 11.8)x^2 + (226.0 \pm 47.1)x - (215.3 \pm 45.5), R = 0.97 \qquad (3.16)$$

3.2 Calculating Rotational Velocity Values

The final relation found (see Equation 3.16) requires constraints for its use. The average broadening from both the 4501 Å TiII feature and the 4508 Å FeII feature must be used. At least three separate measurements need to be made of each

spectral feature. The FWHM values used to calculate the average value need to be consistent in value, with a small standard deviation. Also, it is evident in Figure 3.9 that $v \sin i$ values less than about 40 km/s and greater than about 150 km/s cannot be determined confidently with this method. Averaging the Rodriguez and Royer $v \sin i$ values for each star resulted in an rms error of 8.619 km/s on the spread in the relation. Dividing this value by the square root of the number of data points gives a centroid error of 1.80 km/s for the relation. This is the error introduced by the spread in the relation. The error is inflated slightly at the edges of the relation, and is negligible compared to the average standard deviation of the $v \sin i$ values used as y-coordinates in the relation. The average standard deviation of the $v \sin i$ values from the two catalogs is 8.1 km/s. This average error of 8.1 km/s can be assumed for a $v \sin i$ value found with this relation. Fekel (1997, 2003) took into account broadening due to macroturbulence, attributing 5 km/s for early F-dwarfs and 3-5 km/s for F subgiants. Effects from macroturbulence were not subtracted from the $v \sin i$ values found for the stars in this study, because the effects are smaller than the errors on the values and would be difficult to determine. Four stars in the reduced data set with no previously published $v \sin i$ values had at least three consistently measured FWHM values for the 4501 Å TiII feature and the 4508 Å FeII feature. Below is an analysis for each of these stars. The calculated projected rotational velocity values for these stars are reported in Table 3.5.

V377 Cephei

V377 Cep was found to have an average spectral broadening of 2.628 Å for the TiII and FeII features. With this broadening value, the relation in Equation 3.16 yielded a $v \sin i$ value of 145.869 km/s.

V509 Persei

V509 Per had an average broadening of 2.568 Å. This broadening yielded a $v \sin i$ value of 141.811 km/s.

Table 3.5.   Calculated $v \sin i$ Values

Star	$v \sin i$ (km/s)
V377 Cep	145.9±8.1
V509 Per	141.8±8.1
V784 Cas	<40
VW Ari	>150

V784 Cassiopeia

The spectral broadening of V784 Cas was found to be 1.506 Å on the low end of the relation in Figure 3.9. The relation yielded a $v \sin i$ value of 31.815 km/s. Since the relation breaks down at a broadening value of about 1.5 Å, this star is reported to be a slow rotator, with a $v \sin i$ value of less than 40 km/s.

VW Ari

A broadening value of 3.087 Å was found for VW Ari. This value is higher than those in the relation given in Equation 3.9. The relation yields a $v \sin i$ value of 153.878 km/s. It is therefore reported as a fast rotator, with a $v \sin i$ higher than 150 km/s.

3.3   Analysis of Hydrogen-Beta Values

Linear regressions were run for both 13 and 15 August 2002, for each filter/calibration combination, plotting the Hβ values calculated by *sbands* against the values found in the Rodriguez et al. (2000) catalog. These plots are given in Figures 3.10 and 3.11. The slopes of the lines in these relations and their corresponding correlation coefficients are given in Table 3.6.

For each filter/calibration combination, the observations for both nights were combined to yield a single relation for each filter/calibration combination. These relations are shown in Figure 3.12. The slopes of the lines in these relations and their corresponding correlation coefficients are given in Table 3.7. The spread in these
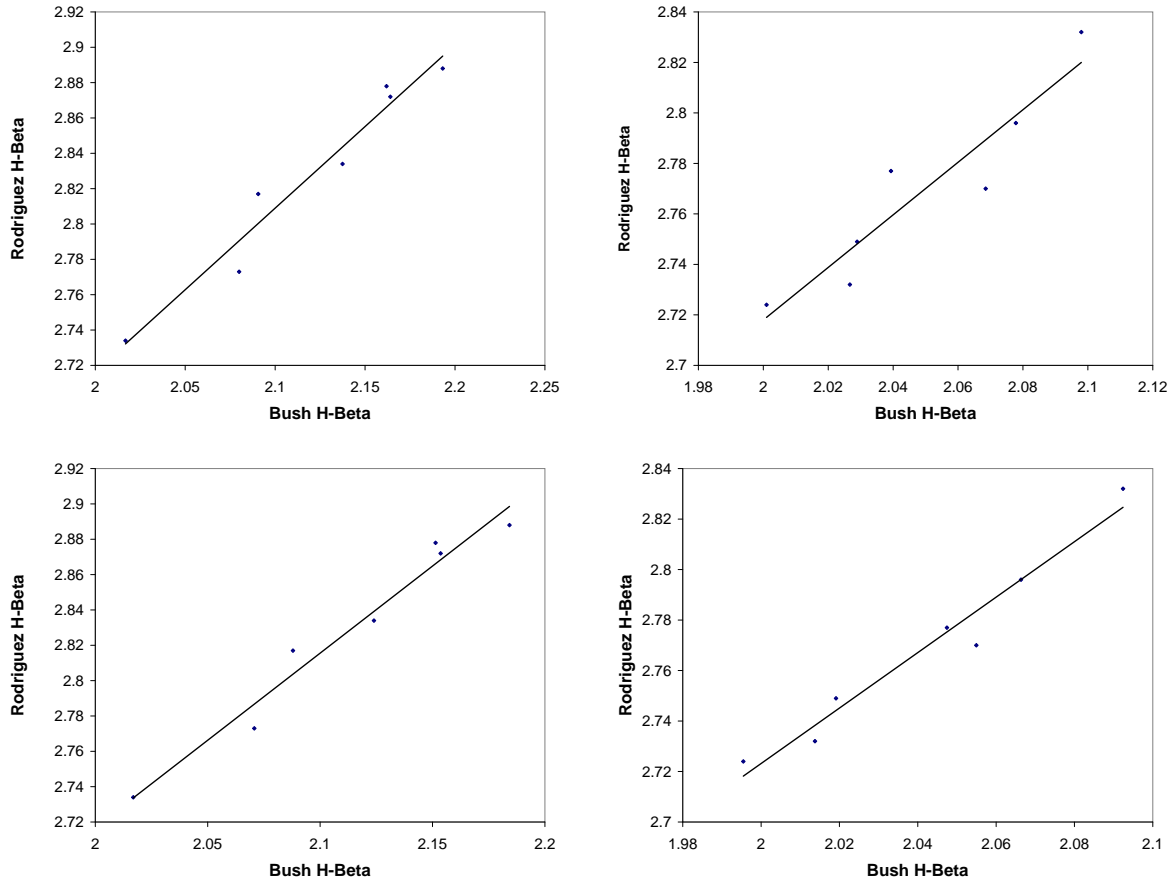
Figure 3.10: Hβ square filter relations for non continuum-calibrated spectra on 13 August 2002 (*top-left*), non continuum-calibrated spectra on 15 August 2002 (*top-right*), continuum-calibrated spectra on 13 August 2002 (*bottom-left*), and continuum-calibrated spectra on 15 August 2002 (*bottom-right*).

Table 3.6.   Relations for Filter/Calibration Combinations for Each Observing Night

Filter	Calibration	Night	Line Slope	Correlation
Square	Non-Continuum	13 Aug	0.923	98%
Square	Non-Continuum	15 Aug	1.041	94%
Square	Continuum	13 Aug	0.985	98%
Square	Continuum	15 Aug	1.098	98%
Gaussian	Non-Continuum	13 Aug	0.924	98%
Gaussian	Non-Continuum	15 Aug	0.878	87%
Gaussian	Continuum	13 Aug	0.978	99%
Gaussian	Continuum	15 Aug	1.083	98%
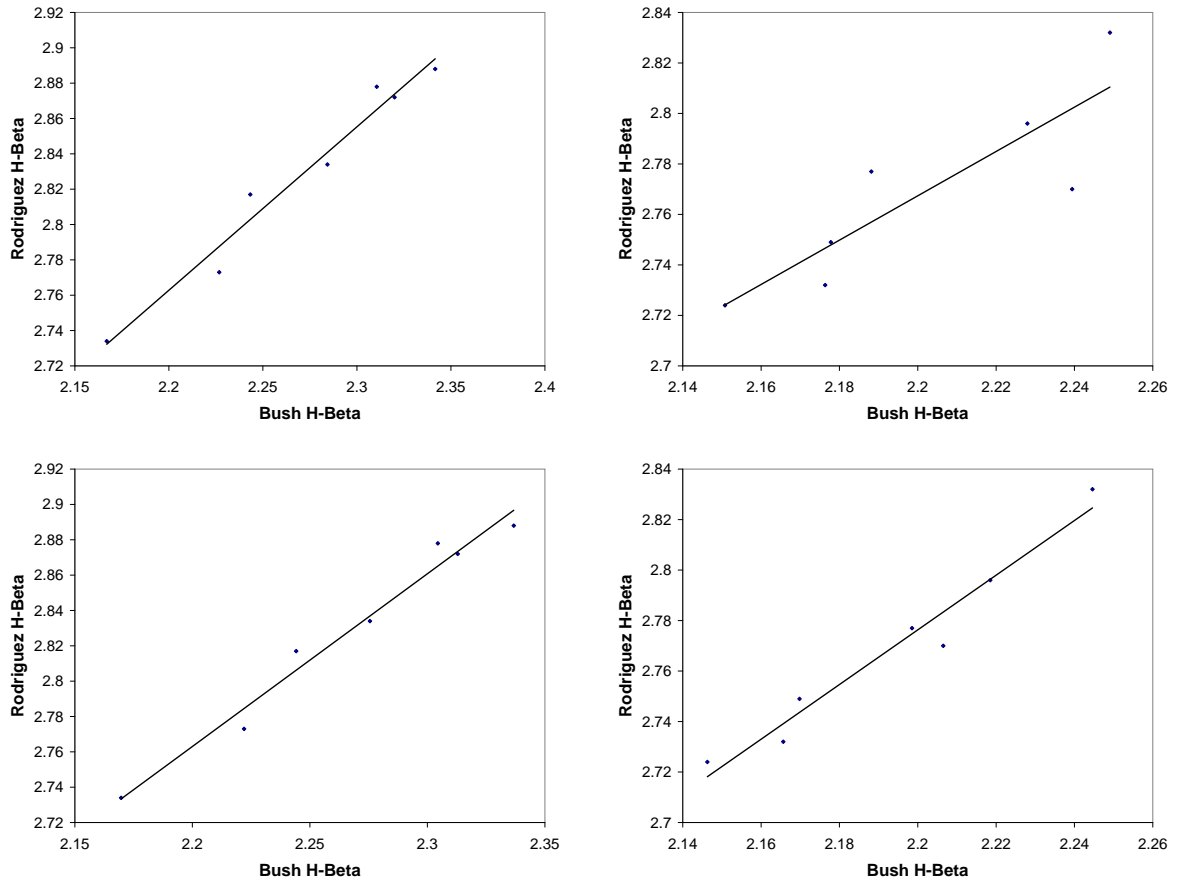
Figure 3.11: Hβ Gaussian filter relations for non continuum-calibrated spectra on 13 August 2002 (*top-left*), non continuum-calibrated spectra on 15 August 2002 (*top-right*), continuum-calibrated spectra on 13 August 2002 (*bottom-left*), and continuum-calibrated spectra on 15 August 2002 (*bottom-right*).
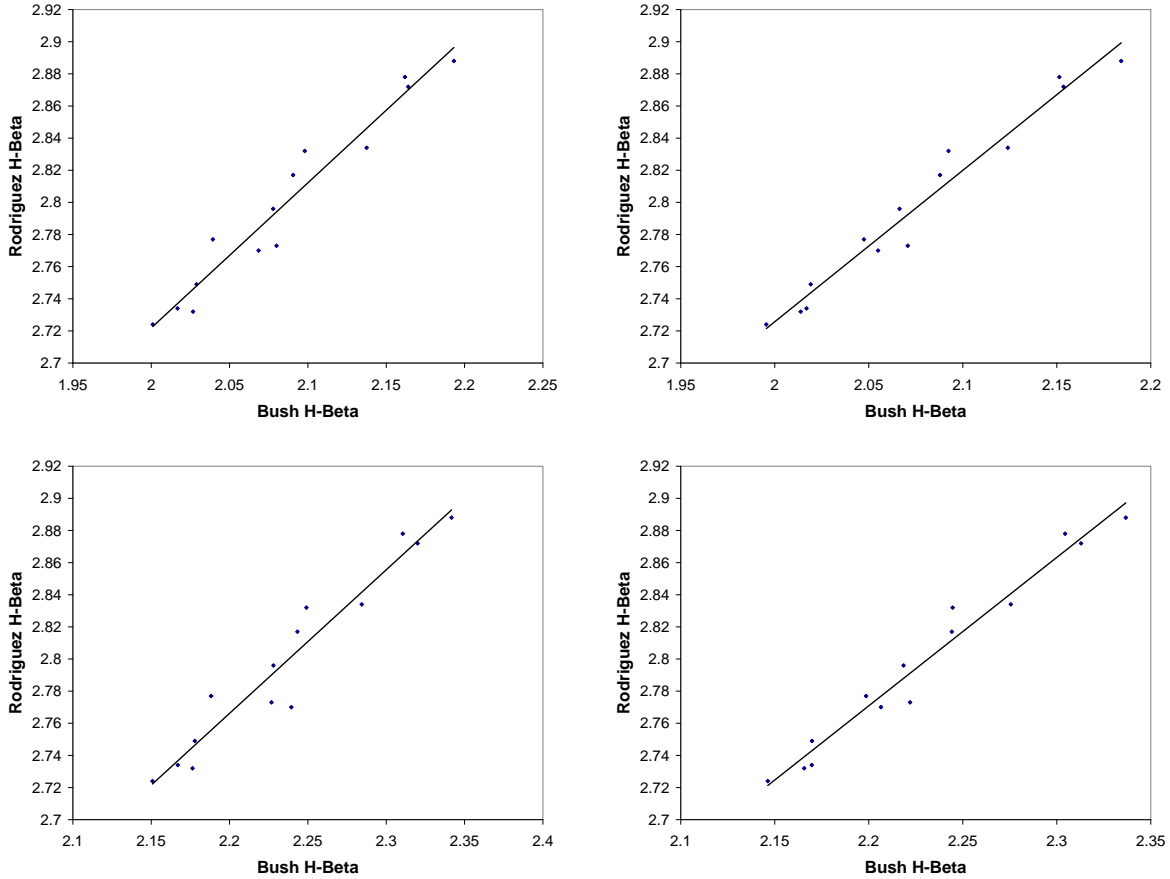
Figure 3.12: Combination of observations from 13 and 15 August 2002 for square Hβ filter non continuum-calibrated spectra (*top-left*), square Hβ filter continuum-calibrated spectra (*top-right*), Gaussian Hβ filter non continuum-calibrated spectra (*bottom-left*), and Gaussian Hβ filter continuum-calibrated spectra (*bottom-right*).

relations could be due to the fact that these stars are variable and their temperatures are changing periodically.

The filter/calibration combination using the square filter with the continuum-calibrated spectra yielded the best relation, with a slope closest to unity and a high correlation, as shown in Equation 3.17. The variable y represents the standardized Hβ value found from the relation, and x represents the raw Hβ value found with *sbands*. Overall, the continuum-calibrated spectra seemed to work better in the Hβ calculations than the non continuum-calibrated spectra.

Table 3.7.   Combined Relations for Filter/Calibration Combinations

Filter	Calibration	Line Slope	Correlation
Square	Non-Continuum	0.903	97%
Square	Continuum	0.942	98%
Gaussian	Non-Continuum	0.894	97%
Gaussian	Continuum	0.924	98%

$$y = (0.942 \pm 0.051)x + (0.842 \pm 0.107), R = 0.98 \qquad (3.17)$$

3.4   Calculating Hydrogen-Beta Values

For the five stars in the reduced data set that did not have previously published Hβ values, measurements were made with *sbands*, and the relation in Equation 3.17 was used as a calibration relation to find final values. These values are reported in Table 3.8. A t-test with a linear fit on the relation given in Equation 3.17 yielded an rms error per data pair of 0.0126 mag and a centroid error of 0.0035. This results in a net error of 0.0131 mag for the relation. This error was assumed for the entire relation, although it would be inflated at the ends of the relation. The Hβ value found for CX Ursae Majoris is higher than are seemingly accepted values for Hβ indices. This may be a clue as to why a value for this star has not been determined in the past. This high value may also be an indication that the calibration used to find Hβ values for all of these stars may be erroneous or that the spectra used still contained some noise.

61

Table 3.8. Hβ Color Index Values for Stars with No Previously Published Values

Star	Raw Hβ Values	Calibrated Hβ Values	Averaged Hβ Value
CN Dra	2.004	2.729±0.013	2.717
	1.982	2.709±0.013	
	1.985	2.711±0.013	
CO Lyn	1.986	2.713±0.013	2.704
	1.967	2.695±0.013	
CX UMa	2.351	3.057±0.013	3.087
	2.415	3.117±0.013	
V377 Cep	2.039	2.762±0.013	2.735
	1.982	2.708±0.013	
V784 Cas	1.930	2.660±0.013	2.656
	1.920	2.650±0.013	
	1.928	2.658±0.013	

Chapter 4

Conclusions

In order to better understand the evolution and structure of δ Scuti stars, this study developed a method for calculating rotational velocity values and Hβ color index values for a large set of data in hand. Spectroscopic observations were taken, and methods for spectral reduction and projected rotational velocity analysis were developed and implemented on a subset of the data. A method for calculating $v \sin i$ values from spectra was developed, and projected rotational velocity values were found for four stars with previously unknown values. Hβ index values were also measured and calibrated with values already in the literature.

Project Limitations

A few key things were learned in this study about developing these methods. The first is that the method development was not as simple as it first appeared. Several iterations and statistical analyses had to be performed in order to develop useful relations. Some spectral features were better used than others to measure rotational broadening. Second, it was critical that the spectra used were reduced correctly and were free of cosmic-ray hits and other artificial features. This was particularly important for the Hβ analysis. Any noise in the spectra was mistaken for spectral features and went into the color index calculations. Lastly, it is difficult to do these analyses for variable stars because the temperatures of these stars change periodically, making it difficult to assign them color index values. In order to make more accurate measurements in the future, it would be ideal to have several measurements of the stars spread out over a longer period of time, so they could be measured at different points in their pulsation cycles.

Future Research

The methods developed in this study were only applied to a subset of the data that were taken. The entire data set contains almost twice as many δ Scutis as were used in this development, down to 13th magnitude. Many more gaps in the Rodriguez et al. (2000) catalog can be filled in with the remaining data set, especially for the stars between 7th and 8th magnitudes. Now that the methods are developed, future projects can apply these methods to the fainter magnitude stars. Applying these methods with a greater number of data points should also help to improve upon the relations developed and to increase the accuracy of the calculations made and the data presented.

References

Abney, Capt. W. de W., 1877, MNRAS, 37:278A

Carroll, J. A. 1933, MNRAS, 83:478

Crawford, D. L. 1975, AJ, 80:955-971

Crawford, D. L. 1977, AJ, 83:48-63

Crawford, D. L. 1979, AJ, 84:1858-1865

Crawford, D. L., Mander, J. 1966, AJ, 71:114C

Dall, T. H., Strassmeier, K. G., & Bruntt, H. 2006, Astrophysics and Space Science, 304:195-197

Fekel, F. C. 1997, PASP, 109:514-523

Fekel, F. C. 2003, PASP, 115:807-810

Gray, D. F., 1982, ApJ, 258:201-208

Gray, D. F., 1984, ApJ, 281:719-722

Gray, D. F., 1989, ApJ, 347:1021-1029

McNamara, D. H. 2007, private communications

Rodríguez, E., López de Coca, P., Rolland, A., Garrido, R. & Costa, V., 1994, Astron. Astrophys. Suppl. Ser., 106, 21-28

Rodríguez, E., López González, M. J., &López de Coca, P., 2000, A&AS, 144:469-474

Rorabacher, D. B., 1981, Anal. Chem., 63: 139

Rose, M. B., 2006, Master's Thesis, Brigham Young University

Royer, F., Gerbaldi, M., Faraggiana, R., & Gómez, A. E. 2002a, A&AS, 381: 105

Royer, F., Grenier, S., Baylac, M. O., Bómez, A. E., & Zorec, J. 2002b, A&AS, 393: 897

Shajn, G., & Struve, O., 1929, MNRAS, 89:222S

Slettebak, A., 1949, ApJ, 110:498S

Slettebak, A., 1954, ApJ, 119:146S

Slettebak, A., 1955, ApJ, 121:653S

Slettebak, A. & Howard, R. F., 1955, ApJ, 121:102S

Slettebak, A., Collins II, G. W., Boyce, P. B., White, N. M. & Parkinson, T. D., 1975, The Astrophysical Journal Supplement Series No. 281, 29:137-159

Smith, M. A., Gray, D. F., 1976, PASP, 88:809-823

Struve, O., 1930, ApJ, 72:1S

Taylor, B. J., 2000, A&AS, 362: 563

Zeilik, M. & Gregory, S. A. 1998, "Introductory Astronomy & Astrophysics" (Saunders College Publishing)